Journal of Magnetic Resonance 322 (2021) 106815

Contents lists available at ScienceDirect

Journal of Magnetic Resonance

journal homepage: www.elsevier.com/locate/jmr

SABRE and PHIP pumped RASER and the route to chaos

Stephan Appelt [a,b,*], Sören Lehmkuhl [c,*], Simon Fleischer [b], Baptiste Joalland [d], Nuwandi M. Ariyasingha [d], Eduard Y. Chekmenev [d,e], Thomas Theis [c,f,g]

[a] Central Institute for Engineering, Electronics and Analytics – Electronic Systems (ZEA-2), Forschungszentrum Jülich GmbH, D-52425 Jülich, Germany
[b] Institut für Technische und Makromolekulare Chemie, RWTH Aachen University, D-52056 Aachen, Germany
[c] Department of Chemistry, North Carolina State University Raleigh, NC 27695-8204, USA
[d] Department of Chemistry, Integrative Biosciences (Ibio), Karmanos Cancer Institute (KCI), Wayne State University Detroit, MI 48202, USA
[e] Russian Academy of Sciences, Leninskiy Prospekt 14, Moscow 119991, Russia
[f] Department of Physics, North Carolina State University Raleigh, NC 27695, USA
[g] Joint Department of Biomedical Engineering, University of North Carolina at Chapel Hill & North Carolina State University, Raleigh, NC 27695, USA

ARTICLE INFO

Article history:
Received 30 June 2020
Revised 21 August 2020
Accepted 24 August 2020
Available online 28 August 2020

Keywords:
RASER
Hyperpolarization
NMR spectroscopy
MRI
Parahydrogen
PHIP
PASADENA
ALTADENA
SABRE
Synergetics
Slaving principle
Non-linear coupled oscillators
Mode collapse
Period doubling
Chaos
Intermittence

ABSTRACT

In a RASER (Radio-frequency Amplification by Stimulated Emission of Radiation), the fast relaxing electromagnetic modes of an LC resonator are enslaved by the slow nuclear spin motion, whose coherence decays with the transverse relaxation rate $\gamma_m = 1/T_2^*$. Such a system obeys the slaving principle, mathematically identical with the adiabatic elimination procedure, leading to multi-mode RASER equations. If the pumping rate of nuclear spin polarization $\Gamma >> \gamma_m$, a second adiabatic elimination process applies and the spectral properties of the RASER can be predicted. The resulting model is similar to the model of two non-linear coupled oscillators and predicts the observed RASER phenomena, including frequency combs and mode collapse. If the second adiabatic elimination is not applicable, mode collapse is completely absent and successive period doubling processes and chaos occur at very high population inversions. We compare these theoretical predictions with experimental results from a PHIP (Para-Hydrogen Induced Polarization) pumped ^{1}H RASER. Moreover, in SABRE (Signal Amplification By Reversible Exchange) pumped ^{1}H experiments, RASER revivals are observed long after the parahydrogen pumping source has been switched off. All these findings shed light onto the links between NMR spectroscopy, RASER physics, synergetics and chaos theory. Several new applications are envisioned in the fields of quantum sensor technology, structure investigation or magnetic resonance imaging (MRI).

1. Introduction

Our universe is composed of two different species, fermions with half-integer spins and bosons with integer spins. For composed quantum systems, S. Haroche and J.-M. Raimond [1] have extended the description using spins by adding the concept of springs. For example, the spins can be electrons, nuclear spins or atoms while the springs are the photons in a resonator or the spins can be ions in a trap and the springs are the vibronic states between coupled ions. Two examples where the concept of spins and springs is useful are the LASER and the RASER. In a LASER [2–5] electron spins of atoms in the LASER's active medium are pumped into an inverted state and interact with the photons in an optical resonator ($\sim 10^{14}$ Hz). In a RASER nuclear spins are pumped and oscillate at frequencies of 10^4–10^9 Hz while interacting with low frequency photons in an LC resonator [6–10].

In this perspective article, we explore the non-linear nature of coupled nuclear spins using the methods of NMR spectroscopy [11,12] and synergetics, especially Haken's slaving principle [13,14]. The latter uses an adiabatic elimination of fast variables and can be used to analyze the motion of a coupled spin-spring systems. Specifically, the slowest changing order parameter enslaves the fast-changing degrees of freedom. This leads to an enormous reduction in the number of degrees of freedom for com-

* Corresponding authors at: Central Institute for Engineering, Electronics and Analytics – Electronic Systems (ZEA-2), Forschungszentrum Jülich GmbH, D-52425 Jülich, Germany.
E-mail addresses: st.appelt@fz-juelich.de (S. Appelt), slehmku@ncsu.edu (S. Lehmkuhl).

https://doi.org/10.1016/j.jmr.2020.106815
1090-7807/

plex systems, where many subsystems are coupled. In a LASER, the slow changing parameter is the light field intensity (the photons) in the optical resonator. This slow changing light field enslaves the electronic spins in atoms, which are pumped and relax very fast compared to the rate of change in the light field. In contrast, for the RASER it is the nuclear spins that enslave the photons of the LC resonator, because the longitudinal and transverse spin states change slowly compared to the decay rate of the photon number in the LC resonator [8].

In this article, the central focus is theoretical and experimental analysis of the single-mode, two-mode and multi-mode RASER in the time and frequency domain. The theory is presented in Sections 2–4. Section 2 introduces the general multi-mode RASER equations. Section 3 presents dynamic features of the single-mode RASER in the presence of a time dependent pumping rate $\Gamma(t)$. If the pumping source is switched off and $\Gamma(t)$ decays exponentially, a sequence of several RASER revivals are expected, which we demonstrate here. In Section 4, the motion of the two-mode RASER is analyzed within the frame of the second adiabatic elimination procedure, which applies if the pumping rate Γ is much larger than the transverse relaxation rate $\gamma_m = 1/T_2^*$. Thus, if $\Gamma >> \gamma_m$ holds, then the two-mode RASER spectrum is either a frequency comb or collapses into one single mode (mode locking). This behavior is very similar to the spectral features of two non-linear coupled classical oscillators [15], as discussed in Sections 4.1 and 4.2. However, for most PHIP pumped RASERs in high field, we encounter the opposite case where $\Gamma << \gamma_m$ and the second adiabatic elimination procedure cannot be applied. Therefore, the dynamics of the two-mode RASER differ in striking ways. As outlined in Section 4.3, a change in the splitting between two modes is observed, multiple period doubling arises and chaotic motion ensues. Section 5 describes the experimental setup for the ^{1}H RASER experiments for both, SABRE and PHIP as polarization source. Section 6 provides experimental demonstrations for the RASER revivals, theoretically predicted in Section 3. Specifically, we show that SABRE [16–18] pumped pyrazine molecules exhibit ^{1}H RASER activity long after the parahydrogen (p-H_2) source has been stopped. In Section 7 experimental results with a PHIP [19–22] pumped ^{1}H RASER at high field are presented. The RASER active samples are characterized with standard and PHIP hyperpolarized NMR in Sections 7.1 and 7.2. The following Section 7.3 features RASER experiments using the ALTADENA protocol (Adiabatic Longitudinal Transport After Dissociation Engenders Nuclear Alignment). These experimental RASER spectra stem from a complex spin system, nonetheless, they show the basic non-linear features predicted in Section 4 using only a two-mode model. The contrast between experiment and simulation is highlighted in Fig. 8. Section 7.4 presents results of ^{1}H RASER experiments based on the PASADENA protocol (Parahydrogen And Synthesis Allow Dramatically Enhanced Nuclear Alignment). These observed RASER spectra contain chemical shift and J-coupling information accompanied with period-doubling and intermittence phenomena, as is immediately apparent from Fig. 9. Section 8 concludes this article, while Section 9 envisions future perspectives and applications for RASER based NMR spectroscopy.

2. The multi-mode RASER equations

Recently, the multi-mode RASER equations have been derived [8] on the basis of Haken's LASER theory [5,13,14]. An important step for the derivation is the first adiabatic elimination process, which states that the fast changing electromagnetic RASER modes follow the slowly changing transverse NMR spin modes of the RASER. For RASER active protons in liquids this means that the electromagnetic field modes with complex amplitude b_m of the RASER resonator change at a rate $\kappa_m = \omega_0/Q = 10^3 - 10^6\ s^{-1}$ (ω_0 = angular Larmor frequency, Q = quality factor ~ 100), which is much larger than the effective transverse relaxation rate $\gamma_m = 1/T_2^* \sim 1s^{-1}$ (T_2^* = effective transverse relaxation time). Because $\kappa_m >> \gamma_m$ is valid, the electromagnetic field mode b_m can be eliminated by the slaving principle [8]. This leads, for N RASER modes, μ, to a set of 2 N coupled differential equations for the population inversions $d_\mu(t)$ and the transverse spin components defined as $\alpha_\mu(t) = A_\mu(t)\exp\left(i\phi_\mu(t)\right)$. The real valued phases $\phi_\mu(t)$ and the amplitudes $A_\mu(t)$ are functions of time t. For the sake of clarity we omit the time variable t in of $d_\mu(t)$, $A_\mu(t)$ and $\phi_\mu(t)$ and simply write d_μ, A_μ and ϕ_μ. When separating the real and imaginary parts of the transverse spin components α_μ the equation of motion for $\mu = 1...N$ coupled RASER modes is given by the following set of 3 N coupled first order differential equations for d_μ, A_μ and the phases ϕ_μ.

$$\dot{d}_\mu = \Gamma_\mu(t)(d_{\mu,0} - d_\mu) - \frac{d_\mu}{T_{1,\mu}} - \frac{4|g_m|^2}{\kappa_m}\sum_{\nu,\sigma=1}^{N} A_\nu A_\sigma \cos(\phi_\nu - \phi_\sigma) \quad (1)$$

$$\dot{A}_\mu = -\gamma_m A_\mu + \frac{|g_m|^2}{\kappa_m} d_\mu \sum_{\tau=1}^{N} A_\tau \cos\left(\phi_\tau - \phi_\mu\right) \quad (2)$$

$$\dot{\phi}_\mu = \omega_\mu + \frac{|g_m|^2}{\kappa_m}\frac{d_\mu}{A_\mu}\sum_{\tau=1}^{N} A_\tau \sin\left(\phi_\tau - \phi_\mu\right) \quad (3)$$

Eqs. (1)–(3) constitute the core of the multi-mode RASER theory whose equivalent form with d_μ and α_μ has been derived in [8]. The dots above d_μ, A_μ and ϕ_μ on the left side of Eqs. (1)–(3) denote ordinary derivatives, i.e. $\dot{d}_\mu = \mathrm{d}d_\mu/\mathrm{d}t$, $\dot{A}_\mu = \mathrm{d}A_\mu/\mathrm{d}t$, and $\dot{\phi}_\mu = \mathrm{d}\phi_\mu/\mathrm{d}t$. No partial derivatives are needed since time t is the only independent variable and the dependent variables d_μ, A_μ and ϕ_μ are not functions of a second independent variable such as the space. The splitting of α_μ in two separate equations Eqs. (2) and (3) for the variables A_μ and ϕ_μ serves to emphasize the close connection to classical non-linear coupled oscillators. This will be shown later in Section 4. Eq. (1) describes the pumping process of the population inversion d_μ of mode μ towards the equilibrium population inversion $d_{\mu,0}$ with a pumping rate $\Gamma_\mu(t)$, which in general can be time dependent. The value of $d_{\mu,0}$ is reduced by the longitudinal relaxation process described by $-d_{\mu,0}/T_{1,\mu}$, where $T_{1,\mu}$ is defined as the longitudinal relaxation time for mode μ. The third term on the right side of Eq. (1), given by $-\left(4|g_m|^2/\kappa_m\right)\sum_{\nu,\sigma=1}^{N} A_\nu A_\sigma \cos(\phi_\nu - \phi_\sigma)$, describes a modulation of d_μ by the expression $\cos(\phi_\nu - \phi_\sigma)$, $\nu \neq \sigma$. The squared magnetic coupling constant in SI units is given by $|g_m|^2 = \gamma_X^2 \mu_0 \hbar \omega_0/4V_s$, where γ_X, μ_0, $\hbar$ and *constant and the sample volume, respectively.*$_s$ and V_s are the gyromagnetic ratio of nucleus X, the vacuum magnetic susceptibility, Planck's constant and the sample volume, respectively. For the population inversion is decreased by the term $-\left(4|g_m|^2/\kappa_m\right)A_\mu^2$. Note that in Eqs.(1)–(3) the transverse relaxation rate $\gamma_m = 1/T_2^*$ is assumed to be the same for all μ but the longitudinal relaxation rates $T_{1,\mu}^{-1}$ might differ for different μ. Eq. (2) describes the time evolution of the RASER amplitude A_μ including a term $-\gamma_m A_\mu$ describing an exponential decay and a source term proportional to $\left(|g_m|^2/\kappa_m\right) d_\mu \sum_{\tau=1}^{N} A_\tau \cos\left(\phi_\tau - \phi_\mu\right)$. So, for $\tau \neq \mu$, A_μ is modulated by the term $\cos\left(\phi_\tau - \phi_\mu\right)$ and for $\tau = \mu$ the term $\left(|g_m|^2/\kappa_m\right) d_\mu A_\mu$ acts as a source term which is responsible for

RASER action. The evolution of the phases ϕ_μ as given by Eq. (3) is defined by the off- resonant angular frequencies ω_μ, which characterize the position of the NMR line in the spectrum, and by the expression $\left(|g_m|^2 d_\mu/\kappa_m A_\mu\right) \sum_{\tau=1}^{N} A_\tau \sin\left(\phi_\tau - \phi_\mu\right)$. This is nonzero for $\tau \neq \mu$ and gives rise for non-linear frequency shifts and frequency combs in the corresponding RASER spectrum. The high complexity described by Eqs. (1)–(3) is based on the fact that all variables d_μ, A_μ and ϕ_μ depend on each other in a non-linear way. If $d_{\mu,0}$ is high enough and none of the variables d_μ, A_μ and ϕ_μ can be eliminated by the slaving principle, this leads to a sequence of period doubling processes and to chaotic behavior. An analysis for these various types of complex RASER spectra for the simplest case of two coupled modes will be detailed in Section 4.

3. Single-mode RASER with time dependent pumping rate

Single-mode RASER or MASER dynamics, including initial dynamics under a constant pumping rate Γ (relaxation oscillations), were detailed in previous reports [23–25]. For RASERs pumped by dynamical nuclear polarization (DNP) [26,27] or by spin exchange optical pumping (SEOP) [28–31] the time constant for reaching equilibrium electron spin polarization is usually much less than a ms, while the range of transverse relaxation times for ^{1}H, ^{129}Xe, or ^{3}He nuclear spins may vary from seconds to hours ($\gamma_m < 1\,s^{-1}$) [23–25,32]. In contrast, for nuclear spin systems pumped by *para*-hydrogen, such as SABRE or PHIP, the buildup time for ^{1}H spin polarization in liquids is in the range 10–100 s. This is because the dissolution of parahydrogen (p-H_2) gas into a solvent and the insertion rates of target molecules onto the employed Rh- or Ir-catalyst are comparatively slow. Therefore, after turning off the p-H_2 supply, the SABRE or PHIP pumping process persists much longer in comparison to T_2, and the pumping rate $\Gamma(t)$ decays slowly as a function of time. This difference between the previously studied ^{1}H, ^{129}Xe, or ^{3}He RASER or MASER systems and the PHIP/SABRE pumped RASER is responsible for new effects, which we observe and explain here. According to Eqs. (1)–(3) the dynamics of a single-mode RASER ($N = 1$) is given by three coupled differential equations for d, A and ϕ.

$$\dot{d} = \Gamma(t)(d_0 - d) - \frac{d}{T_1} - 4\frac{|g_m|^2}{\kappa_m}A^2 \tag{4}$$

$$\dot{A} = \left(\frac{|g_m|^2}{\kappa_m}d - \gamma_m\right)A \tag{5}$$

$$\dot{\phi} = \omega_1 \tag{6}$$

There is only one mode oscillating with ω_1 in Eq. (6) without any additional oscillating terms. A RASER threshold can be identified by inspection of Eq. (5). RASER emission starts if the term in brackets of Eq. (5) becomes positive, which means the threshold is $d_{th} = \kappa_m \gamma_m/|g_m|^2$. No exact solution for the system described by Eqs. (4)–(6) exists, so numerical solutions for specific pumping conditions $\Gamma(t)$ have to be used. Assuming a slowly and exponentially increasing pumping rate (after turning on p-H_2) or decaying pumping rate (after turning off p-H_2 source) we express $\Gamma(t)$ as,

$$\Gamma(t) = \Gamma_0\left[1 - \exp(-t/\tau_p)\right] \tag{7}$$

$$\Gamma(t) = \Gamma_0 \exp(-t/\tau_r) \tag{8}$$

where Γ_0 is the maximum possible pumping rate and τ_p and τ_r are defined as the time constants for the pumping or relaxing, respectively. Numerical evaluation of Eqs. (4)–(8) predict that a phenomenon of RASER revivals occurs provided the condition $\tau_p^{-1}, \tau_r^{-1} << \gamma_m$ is met. This means that a sequence of RASER bursts with decreasing intensity is observed long after the pumping process has stopped. The revivals exist until the population inversion has decayed below the RASER threshold. Such RASER revivals are presented and explained in Section 6.

4. Dynamics of the two-mode RASER

In this section, we discuss the complexity that can arise if two RASER modes are non-linearly coupled. After introducing the model of two non-linear coupled classical oscillators (Section 4.1) we derive the equations for a two-mode RASER with identical mode amplitudes (Section 4.2). Based on these equations, two different cases can be distinguished: First, the RASER operates in a regime where the second adiabatic elimination approach can be applied, i.e. $dd/dt = 0$ (Section 4.3). This is realized experimentally if for example $\Gamma >> \gamma_m$. Second, if the RASER operates in a regime, where the above principle is invalid, no collapse into one mode is possible and period doubling or chaos occurs under appropriate conditions (Section 4.4).

4.1. Model of two non-linear coupled oscillators

First we introduce the simplest case of two non-linearly coupled oscillators, which has been discussed by S. H. Strogatz [15]. As shown in Fig. 1(a), two oscillator modes are represented by two rotating masses moving on a unit circle with different angular frequencies ω_1 and ω_2. The position of each bead is determined by the phases ϕ_1 and ϕ_2. A non-linear coupling between the two modes is symbolized by a non-linear spring between the two beads which gives rise to a force like action proportional to $R\sin(\phi_2 - \phi_1)$. In this example, the parameter R is a constant describing the strength of the non-linear coupling and $\sin(\phi_2 - \phi_1)$ is the nonlinearity. (R has the unit [s^{-1}], just like a rate constant, which will be relevant later when comparing the model of two non-linear coupled oscillators with the two-mode RASER.) For this model, the equation of motion for the phase angles ϕ_1 and ϕ_2 is given by

$$\dot{\phi}_1 = \omega_1 + R\sin(\phi_2 - \phi_1), \tag{9}$$

$$\dot{\phi}_2 = \omega_2 - R\sin(\phi_2 - \phi_1). \tag{10}$$

The dynamical features of Eqs. (9) and (10) can be analyzed in a phase portrait by introducing the phase difference $\Psi = \phi_2 - \phi_1$. Subtraction of Eq. (9) from Eq. (10) results in

$$\dot{\Psi} = (\omega_2 - \omega_1) - 2R\sin\Psi \tag{11}$$

The solution of Eq. (11) can be split into two cases: 1. $|\omega_2 - \omega_1| \geqslant 2R$ and 2. $|\omega_2 - \omega_1| < 2R$.

The corresponding phase portraits in the two dimensional $\left(\Psi, \dot{\Psi}\right)$ space for a fixed $|\omega_2 - \omega_1| = 2\pi \cdot 7\,s^{-1} = 44\,s^{-1}$ are shown in four panels I-IV in Fig. 1(b). Panels I-III in (b) represent case 1 for three different values of R, while panel IV represents case 2. For case 1, $\dot{\Psi}$ as a function of Ψ never becomes zero and oscillates sinusoidal with an amplitude of $2R$ around $|\omega_2 - \omega_1|$. No mode lock is possible, because Ψ always changes with time ($\dot{\Psi} \neq 0$). In contrast, for the second case $\dot{\Psi} = 0$ at two specific points $\Psi_{s,u} = \arcsin(|\omega_2 - \omega_1|/2R)$, where Ψ_s is a stable fixed point with fixed phase difference, whereas Ψ_u is an unstable fixed point. The difference between Ψ_s and Ψ_u arises because the slope of $\dot{\Psi}$ is negative at Ψ_s and positive at Ψ_u. Thus, the system will evolve to the stable fix point Ψ_s whereas small fluctuations around the unstable point Ψ_u will drive the system away from Ψ_u. The two

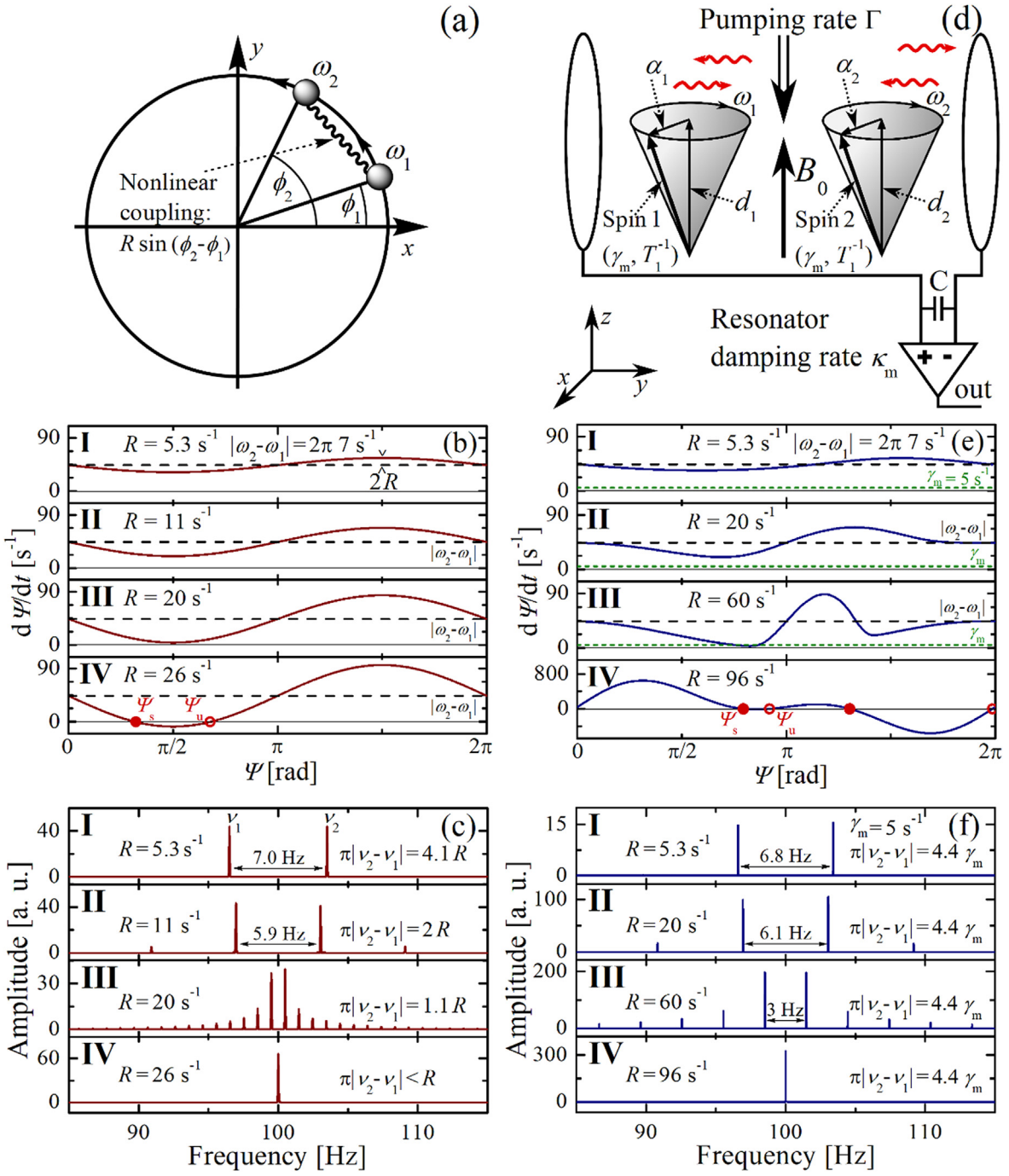

Fig. 1. Comparison of two non-linear coupled oscillators (a-c) and the two-mode RASER (d-f). (a) Two beads at phases ϕ_2 and ϕ_1 rotating with ω_1 and ω_2 are connected by a spring. (b) Phase portrait in the (Ψ, $d\Psi/dt$) -plane for $2R < |\omega_2 - \omega_1|$ (panels I-III) and $2R > |\omega_2 - \omega_1|$ (panel IV). $\Psi = \phi_1 - \phi_2$ and $|\omega_2 - \omega_1| = 2\pi \cdot 7 s^{-1}$ (dashed line). (c) Simulated spectra of (b). While panel I shows only two modes, the frequency combs in panels II and III collapse into one line if $|\nu_2 - \nu_1| < R/\pi$ (panel IV). (d) The two-mode RASER, sketched as two spin species oscillating at ω_2 and ω_1 with the relaxation rates, $\gamma_m = 1/T_2^*$ and T_1^{-1}. The spins are coupled via photons (red arrows) in an LC resonator. (e) Phase portraits in the (Ψ, $d\Psi/dt$)-plane for four different rates R assuming $|\omega_2 - \omega_1| = 2\pi \cdot 7 s^{-1}$ (panels I-IV). The second collapse condition, $\gamma_m = 5\ s^{-1} > \pi|\nu_2 - \nu_1|$, is not fulfilled. (f) Simulated two-mode RASER spectra of (e) at four different values R. All simulated spectra, centered at an off resonance frequency of 100 Hz, are displayed in the absolute mode. Closed and open circles denote stable and unstable fix points Ψ_s and Ψ_u, respectively. (For interpretation of the references to colour in this figure legend, the reader is referred to the web version of this article.)

fix points Ψ_s,Ψ_u for the second case are shown in Fig. 1(b) panel IV, where the range of possible stable or unstable fixed point positions is $0 \leqslant \Psi_s \leqslant \pi/2$ and $\pi/2 \leqslant \Psi_u \leqslant \pi$, respectively.

A useful tool to study nonlinear coupled oscillators is the Fourier analysis, as shown by Borkowski and Stefanski [33]. Four Fourier spectra of the coupled system Eqs. (9) and (10) are shown in Fig. 1(c), where the signal of the two coupled oscillators is $S(t) = \cos\phi_1 + \cos\phi_2$. These four spectra correspond to the four phase diagrams in Fig. 1(b). The spectrum in panel I shows only two lines separated by $|\nu_2 - \nu_1| = 7$ Hz and is simulated for the case $\pi|\nu_2 - \nu_1| = 4.1\,R$ (i.e. $|\omega_2 - \omega_1| = 4.1 \cdot 2R > 2R$) where no fixed points emerge. In panel II, which is simulated for $\pi|\nu_2 - \nu_1| = 2R$ a frequency comb like spectrum with two sidebands is observable. The two sidebands arise due to the increased modulation depth

$D_{\mathrm{mod}} = R/|\omega_2 - \omega_1|$, as discussed in [8]. The distance between consecutive lines (5.9 Hz) is smaller than 7 Hz, which is caused by the non-linear coupling term $R\sin(\phi_2 - \phi_1)$ in Eqs. (9) and (10). This decrease in the observed splitting should not be confused with cavity pulling effects, where modes are shifted differently due to their respective distance to the LC resonance frequency [34]. In panel III, $\pi|\nu_2 - \nu_1| = 1.1\,R$, which is close to the point of collapse $\pi|\nu_2 - \nu_1| = R$. The modulation depth is further increased, which results in a frequency comb with multiple lines spaced much less than 7 Hz. The spectrum in panel IV shows only one line, since the collapse happens at $\pi|\nu_2 - \nu_1| < R$. The modulation depth is so large that a stable fix point Ψ_s exists (Fig. 1(b), panel IV).

4.2. Exact two-mode RASER equations

We proceed by comparing the above model of two non-linearly coupled oscillators (Fig. 1(a – c)) with two coupled RASER modes (see Fig. 1(d – f)), where the second adiabatic elimination process is applied. The model of the two RASER modes is sketched in Fig. 1(d): Two spin species characterized by their angular frequencies ω_1 and ω_2 are pumped with the rate Γ into a state of negative spin polarization. The negative polarizations correspond to the positive valued population inversions d_1 and d_2 with an orientation parallel to the magnetic field B_0. The two values d_1 and d_2 together with the corresponding oscillating transverse spin components $\alpha_1 = A_1\exp(i\,\phi_1)$ and $\alpha_2 = A_2\exp(i\,\phi_2)$ form two cones, which represent the ensemble of two RASER active spin species. The two angular eigenfrequencies ω_1 and ω_2 around the field B_0 are modified by the non-linear coupling into the new angular rates $\dot{\phi}_1$ and $\dot{\phi}_2$. This coupling between the spins and the coil is mediated by the photons (red arrows). The dissipative processes destroying population inversion and phase coherence are characterized by the longitudinal and transverse relaxation rates T_1^{-1} and $\gamma_m = 1/T_2^*$, respectively. The coil and a tunable capacitor form an LC resonator tuned to the resonance frequency $\omega_0 = \gamma_H B_0$. The loss of the LC resonator is characterized by the damping rate $\kappa_m = \omega_0/Q$, (Q = quality factor).

An analysis of this coupled system is possible by using Eqs. (1)–(3) for $N = 2$ and for two identical modes. The latter means $\Gamma_1 = \Gamma_2 = \Gamma$, $T_{1,1} = T_{1,2} = T_1$, $\gamma_m = 1/T_2^*$ for the pumping and relaxation constants and $d_1 = d_2 = d$, $d_{1,0} = d_{2,0} = d_0$, $A_1 = A_2 = A$ for the variables characterizing the spin states. The dynamics of the two RASER modes can now be reformulated by introducing the phase difference $\Psi = \phi_2 - \phi_1$:

$$\dot{d} = \Gamma(d_0 - d) - \frac{d}{T_1} - \frac{8|g_m|^2}{\kappa_m}A^2(1+\cos\Psi) \tag{12}$$

$$\dot{A} = \left(\frac{|g_m|^2 d}{\kappa_m} - \gamma_m\right)A + \frac{|g_m|^2\,d}{\kappa_m}\cos\Psi \tag{13}$$

$$\dot{\Psi} = (\omega_2 - \omega_1) - \frac{2\,|g_m|^2}{\kappa_m}\,d\,\sin\Psi \tag{14}$$

4.3. Second adiabatic elimination and line collapse

The three coupled differential equations Eqs. (12)–(14) form the basis for the two-mode RASER. They can be simplified further, if a condition for a second adiabatic elimination holds, which is the case if in Eq. (12) $\mathrm{d}d/\mathrm{d}t = 0$.

This condition depends on the time constants in Eqs. (12)–(14), which are γ_m, Γ, T_1^{-1}. In liquids and gases at low magnetic fields $T_1 \approx T_2^*$ so $\gamma_m \approx T_1^{-1}$ are of the same order of magnitude. Such a case where $\gamma_m \approx \Gamma \approx T_1^{-1}$ is discussed in [8]. However, in most high field NMR experiments, $T_1 >> T_2^*$ and thus $T_1^{-1} << \gamma_m$. Therefore, at high magnetic fields, three relevant cases can be considered for NMR RASER experiments: $\Gamma << \gamma_m$, $\Gamma \approx \gamma_m$ and $\Gamma >> \gamma_m$. In the case of $\Gamma >> \gamma_m$ the second adiabatic elimination process can be applied. If we set $\mathrm{d}d/\mathrm{d}t = 0$ in Eq. (12), we obtain the following expression for d:

$$d = \frac{\Gamma\,d_0}{\left(\Gamma + T_1^{-1}\right)} - \frac{8|g_m|^2}{\kappa_m\left(\Gamma + T_1^{-1}\right)}A^2(1+\cos\Psi) \tag{15}$$

The population inversion d follows the slowly varying amplitude A and phase difference Ψ. Inserting Eq. (15) into Eqs. (13) and (14) eliminates d and a set of two coupled equations for A and Ψ remains,

$$\dot{A} = [R(1+\cos\Psi) - \gamma_m]\,A - 2L(1+\cos\Psi)^2\,A^3 \tag{16}$$

$$\dot{\Psi} = (\omega_2 - \omega_1) - \left(2R - 4LA^2\right)\,\sin\Psi + 2LA^2\,\sin 2\Psi \tag{17}$$

The two parameters in Eqs. (16) and (17) are the rates $R = |g_m|^2 d_0\,\Gamma/\left[\kappa_m\left(\Gamma + T_1^{-1}\right)\right]$ and $L = 4|g_m|^4/\left[\kappa_m^2\left(\Gamma + T_1^{-1}\right)\right]$ where both R and L have the unit [s $^{-1}$] (just as in the model of two non-linear coupled oscillators of Section 4.1). Note that A and Ψ in Eqs. (16) and (17) span a two-dimensional space. According to the Poincare Bendixson theorem [15], chaos cannot exist in two dimensions, at least three dimensions are necessary for chaotic motion. This is the case in Eqs. (12)–(14) for the three parameters d, A and Ψ, before second adiabatic elimination. The one-dimensional case is known from the model of the two non-linear coupled oscillators (see. Eq. (11)), where Ψ is the only variable and the amplitude A is constant.

As discussed in Section 3, a threshold condition can be identified by looking at the first bracket on the right side of Eq. (16). RASER activity starts if the time average $\langle R(1+\cos\Psi)\rangle > \gamma_m$. At threshold, the term $\langle\cos\Psi\rangle = 0$, since $\Psi \approx (\omega_2 - \omega_1)\,t$ and the threshold condition is reduced to $R = \gamma_m$. The corresponding phase portraits with a sinusoidal modulation in panel I in Fig. 1(e) is very similar to panel I in Fig. 1(b). Further away from threshold, $R > \gamma_m$, the phase portraits in panels II and III of Fig. 1(e) differ from panels II and III of Fig. 1(b). The corresponding phase portraits of panels II and III are obtained by evaluating A, Ψ versus time based on numerical simulations of Eqs. (16) and (17). The distortion of the phase portraits from a sinusoidal stems from the two terms $\left(2R - 4LA^2\right)\sin\Psi$ and $LA^2\sin 2\Psi$ in Eq. (17) where the term LA^2 can no-longer be neglected.

If R is large enough, then $\dot{\Psi} = 0$ at both stable and unstable fixed points Ψ_s, Ψ_u, respectively, as sketched in panel IV of Fig. 1(e). The values of Ψ_s and Ψ_u lie in the range $\pi/2 \leqslant \Psi_s, \Psi_u < \pi$, which differs from panel IV of Fig. 1(b), where $0 < \Psi_s < \pi/2$ and $\pi/2 \leqslant \Psi_u < \pi$. Two other fix points, indicated by closed and open circles, exist in the range $\pi \leqslant \Psi_{s,u} < 2\pi$, which constitute another possibility for mode locking. A line collapse occurs at the stable and time independent fix point Ψ_s. A constant Ψ_s forces the amplitude A in Eq. (16) to evolve into a stationary time independent state A_s. By setting $\mathrm{d}A/\mathrm{d}t = 0$ in Eq. (16) the stationary amplitude A_s is given by

$$A_S = \sqrt{\frac{R(1+\cos\Psi_s) - \gamma_m}{2L(1+\cos\Psi_s)^2}}. \tag{18}$$

Inserting A_s into Eq. (17) and using $\mathrm{d}\Psi/\mathrm{d}t = 0$, an equation for Ψ_s is obtained.

$$\frac{\sin\Psi_s}{(1+\cos\Psi_s)} = \frac{(\omega_2 - \omega_1)}{2\,\gamma_m} \tag{19}$$

Eq. (19) is a transcendent equation for Ψ_s and does not depend on R. A line collapse always occurs, i.e. one fix point Ψ_s exists for every value of the ratio $(\omega_2-\omega_1)/2\gamma_m$ on the right side of Eq. (19). If $|\omega_2-\omega_1|>2\gamma_m$, and consequently $|\nu_2-\nu_1|>\gamma_m/\pi$, the value of Ψ_s is fixed within the range $\pi/2\leqslant\Psi_s\leqslant\pi$, as panel IV in Fig. 1(e) suggests.

We conclude this subsection with the similarities and differences between the two cases, i.e. the two coupled oscillators (Fig. 1(a)–(c)) and the two mode RASER (Fig. 1(d)–(f)). Both cases have comparable phase diagrams for $R<<|\omega_2-\omega_1|$. The spectra show similar features, including frequency combs and line collapse at certain values of R. Furthermore, a decreasing splitting between the two modes with increasing R is common for both cases.

Besides the similarities there are striking differences: A finite $\gamma_m>0$ exist for case 2 with an associated RASER threshold condition $R>\gamma_m$. Therefore R cannot be arbitrarily small as in case 1. Furthermore, the sinusoidal phase diagram of case 1 is distorted and the collapse condition is shifted to higher values of R due to the terms $\left(2R-4LA^2\right)\sin\Psi$ and $LA^2\sin 2\Psi$ in Eq. (17). Finally, there is another possible condition for a line collapse for the RASER: if the separation in frequency space of two RASER lines is smaller than the linewidth, i.e. $|\nu_2-\nu_1|<\gamma_m/\pi$ ($|\omega_2-\omega_1|<2\gamma_m$), the spectrum collapses into one line irrespective of the size of R. In this case the stationary phase Ψ_s is fixed within $0<\Psi_s<\pi/2$.

In the following section we elaborate what happens if the second adiabatic elimination process cannot be applied. Then, a line collapse is completely absent and multiple period doubling processes and chaotic spectra can occur instead.

4.4. RASER without 2nd adiabatic elimination, the route to chaos

In this section, we explore the regime where the second adiabatic elimination procedure cannot be applied, for example when $\Gamma<<\gamma_m$. As stated by Haken [13,14], if the slaving principle breaks down phenomena like period doubling, chaos and intermittence may occur. We concentrate the following analysis of a two-mode RASER observed under experimental conditions encountered in hydrogenative PHIP pumped ^{1}H RASER experiments. In regimes where the slaving principle does not apply the condition $\mathrm{d}d/\mathrm{d}t=0$ as used in Eq. (12) is not valid. Therefore, the phase difference $\Psi=\phi_2-\phi_1$ can never settle at a fixed value but remains time dependent. All three variables d,A,Ψ in Eqs. (12)–(14) are time dependent and mode collapse is impossible.

A proper analysis, where period doubling and chaos arise, is still possible by numerical simulations of Eqs. (12)–(14), which are performed and summarized in Fig. 2. In these simulations, the frequency separation $|\nu_2-\nu_1|$ is set to a fixed value and the equilibrium population inversion d_0 is varied over three orders of magnitude ($d_{th}<d_0<10^3\,d_{th}$). In Fig. 2 different simulated ^{1}H RASER spectra and corresponding signals (insets) are presented based on relaxation and pumping rate parameters $T_2^*=0.13\,\mathrm{s}$, $T_1=16\,\mathrm{s}$ and $\Gamma=0.07\ \mathrm{s}^{-1}$, matching experimental parameters measured in high-field RASER experiments [9]. The spectra and signals in Fig. 2(a)–(d) are simulated for a fixed frequency separation $|\nu_2-\nu_1|=2\,\mathrm{Hz}$ and for four different values of d_0. Note that $|\nu_2-\nu_1|=2\ \mathrm{Hz}<1/(\pi T_2^*)=2.45\ \mathrm{Hz}$, which means the line separation is smaller than the linewidth, $\gamma_m/\pi=2.45\,\mathrm{Hz}$. According to Fig. 1(h), panel I, which uses the adiabatic elimination, a collapse into one line is expected. Instead in Fig. 2(a) with $d_0=9\cdot10^{16}$, we observe a frequency comb with a main line at 200 Hz offset and a separation of 0.3 Hz between two consecutive lines. The corresponding RASER signal (inset) consists of a regular series of pulses with constant maximal amplitude. At higher population inversion $d_0=1.5\cdot10^{17}$(Fig. 2(b)) the spectrum becomes more complex, consisting of a frequency comb with 0.4 Hz line separation between two main lines and seven smaller lines located between each pair of large lines (i.e. threefold period doubling). All separations in frequency space between the small lines inside in a group are 0.05 Hz, 0.1 Hz, 0.2 Hz and 0.4 Hz. The whole spectrum can be explained by threefold period doubling, where the separation of 0.4 Hz/2 = 0.2 Hz represents the first period doubling occurrence while 0.4 Hz/2^2 = 0.1 Hz and 0.4/2^3 = 0.05 Hz represent the second and third period doubling. With further increasing population inversion, at $d_0=3\cdot10^{17}$ (Fig.(2c)), the spectrum is composed of several groups separated by about 0.5 Hz while each group consists of many lines with a minimum distance of about 0.02 Hz. Smaller values than 0.02 Hz cannot be observed since the chosen Hamming window limits the resolution (200 s, line width ~10 mHz). More lines with a minimum separation smaller than 0.02 Hz appear, if the window is chosen larger than 200 s. The corresponding RASER signal (inset) shows a sequence of RASER bursts, where the maximum amplitude of each burst changes in irregular ways. This indicates the onset of the chaotic regime. We applied numerical tests proving chaos such as the exponential explosion of two nearby RASER trajectories [13–15]. At the high value $d_0=1.4\cdot10^{19}$ (Fig. 2(d)) the chaos disappears and the RASER spectrum is once again a frequency comb with 4.4 Hz separation between two consecutive lines.

The situation is quite different for the case $|\nu_2-\nu_1|=7\,\mathrm{Hz}>\gamma_m/\pi=2.45\,\mathrm{Hz}$, as presented in Fig.(2e-h). At low population inversion $d_0=9\cdot10^{16}$ the RASER spectrum (e) is a doublet whose lines are separated by 7.2 Hz, which is close to the frequency separation $|\nu_2-\nu_1|=7\,\mathrm{Hz}$. At $d_0=1.4\cdot10^{19}$ the RASER spectrum in Fig. 2(f) shows chaotic features. The corresponding RASER signal (inset) is characterized by irregular and chaotic bursts and differs significantly from the signal in (c). At $d_0=2\cdot10^{19}$(g), no chaotic spectrum exists; instead, a frequency comb is visible with a separation of 7.6 Hz between two consecutive large peaks and smaller lines located at exactly half the separation of 7.6 Hz. This represents a period doubling process. The corresponding signal in the inset is a regular sequence of RASER bursts with alternating amplitude. At $d_0=4\cdot10^{19}$ (h) the period doubling has stopped and the spectrum is reduced to a frequency comb with 9.9 Hz line separation.

A global overview of all possible frequency separations between consecutive lines versus the equilibrium population inversion d_0 is shown in Fig. (3). The graph has been calculated through the simulation of 120 RASER spectra for three different frequency separations $|\nu_2-\nu_1|=7\,\mathrm{Hz}$ (circles), 3.5 Hz (diamonds) and 2 Hz (squares). In all three plots, the frequency separation increases with d_0, as already shown in Fig. 2 for a few examples. This is in stark contrast to the decreasing line separation outlined in Section 4.2 (see Fig. 1). The reason for this contrast is not clear yet.

For $|\nu_2-\nu_1|=7\,\mathrm{Hz}$ (Fig. 3, blue circles), the separation between two modes stays close to (only slightly above) 7 Hz for a large range $4.5\cdot10^{16}<d_0<10^{19}$.

In the region $1.33\cdot10^{19}<d_0<1.5\cdot10^{19}$ the RASER spectrum shows chaotic features (blue polygon in Fig. 3), which is characterized by a continuum of frequency differences. For higher values at $1.5\cdot10^{19}<d_0<2.5\cdot10^{19}$ the chaos subsides and the spectrum is characterized by a one-fold period doubling. For example, at $d_0=2.5\cdot10^{19}$, a third line appears exactly in-between the two lines separated by 9.3 Hz, i.e. at 4.15 Hz. This is represented in the plot as a second circle plotted below the first circle at 9.3 Hz. For $d_0>3\cdot10^{19}$ the one-fold period doubling vanishes and the spectrum reduces to a frequency comb with many sidebands and

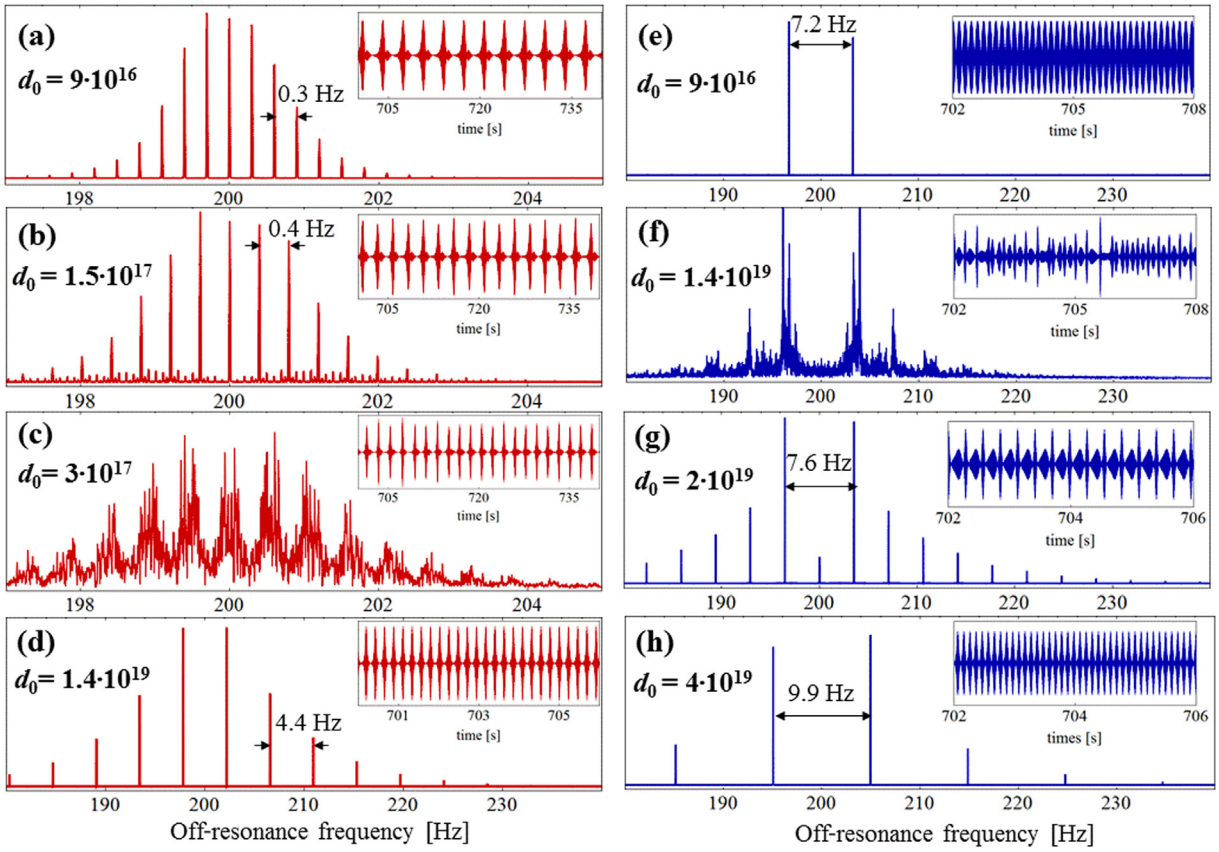

Fig. 2. Simulations of two-mode ^{1}H RASER spectra and time dependent signals (insets) for two, fixed frequency differences $|\nu_2 - \nu_1| = 2$ Hz (a–d) and $|\nu_2 - \nu_1| = 7$ Hz (e-h) at different equilibrium population inversions d_0. (a) Close to the threshold at $d_0 = 9 \cdot 10^{16}$, a frequency comb with 0.3 Hz line separation appears. (b) At $d_0 = 1.5 \cdot 10^{17}$, a frequency comb with three-fold period doubling is observed. (c) At $d_0 = 3 \cdot 10^{17}$ a spectrum with a manifold of lines indicating chaos is observed. (d) At $d_0 = 1.4 \cdot 10^{19}$, the spectrum reduces again to a frequency comb. In (e), $d_0 = 9 \cdot 10^{16}$, two lines split by 7.2 Hz appear, close to $|\nu_2 - \nu_1| = 7$ Hz. (f) At $d_0 = 1.4 \cdot 10^{19}$, the spectrum and the RASER signal (inset) display chaotic features. (g) At $d_0 = 2 \cdot 10^{19}$, the spectrum becomes a frequency comb including one-fold period doubling. (h) Finally, at $d_0 = 4 \cdot 10^{19}$, an even frequency comb without period doubling is observed.

with increasing mode separation reaching 10 Hz at $d_0 = 10^{20}$. We found that no further period doublings or chaos exists up to $d_0 = 10^{21}$.

For $|\nu_2 - \nu_1| = 3.5$ Hz (black diamonds) and for $d_0 = 5 \cdot 10^{16}$ close to the threshold at $d_{th} = 4.5 \cdot 10^{16}$ the frequency separation is 2.51 Hz (below the original spectral separation of 3.5 Hz). With increasing d_0 the frequency separation grows slowly and reaches 2.87 Hz at $d_0 = 10^{18}$. In the range $2 \cdot 10^{18} < d_0 < 2.5 \cdot 10^{18}$ a one-fold period doubling occurs. For values $2.6 \cdot 10^{18} < d_0 < 4.5 \cdot 10^{18}$ the spectrum is chaotic (black polygon). In the narrow range $4.7 \cdot 10^{18} < d_0 < 6 \cdot 10^{18}$ the spectrum is characterized by a three-fold period doubling. For example at $d_0 = 4.7 \cdot 10^{18}$ the observed frequency separations are 3.2 Hz, 1.6 Hz, 0.8 Hz and 0.4 Hz. In the range $6 \cdot 10^{18} < d_0 < 8 \cdot 10^{18}$ the spectrum reduces to a one-fold period doubling and for $d_0 > 9 \cdot 10^{18}$ all spectra are frequency combs.

For $|\nu_2 - \nu_1| = 2$ Hz (red squares) and in the range $5 \cdot 10^{16} < d_0 < 9 \cdot 10^{16}$ the spectrum is dominated by a frequency comb, whose spacings ranging from 0.16 Hz at $d_0 = 5 \cdot 10^{16}$ to 0.3 Hz at $d_0 = 9 \cdot 10^{16}$ are much less than $|\nu_2 - \nu_1| = 2$ Hz. Note that there is no line collapse although $|\nu_2 - \nu_1| = 2$ Hz $< 1/(\pi T_2^*) = 2.45$ Hz. At $10^{17} < d_0 < 1.3 \cdot 10^{17}$ one-fold period doubling is observed, which for $1.3 \cdot 10^{17} < d_0 < 1.6 \cdot 10^{17}$ transforms into a three-fold period doubling. The chaotic regime (red polygon) follows at $1.6 \cdot 10^{17} < d_0 < 3.5 \cdot 10^{17}$. In the region $3.5 \cdot 10^{17} < d_0 < 5 \cdot 10^{17}$ two-fold period doubling occurs and at $5 \cdot 10^{17} < d_0 < 2 \cdot 10^{18}$ turns into a one-fold period doubling. Finally, at $d_0 > 2 \cdot 10^{18}$ all period doublings have gone and the spectrum reduces to a frequency comb. The whole picture is similar to situations describe by bifurcation theory and plotted in bifurcation diagrams, e.g. the logistic map [15]. In general, bifurcation theory is used to describe dynamical systems that respond to a small smooth change made to one parameter (the bifurcation parameter) with a sudden topological change. In the specific case of the logistic map, which uses a growing factor r comparable effects are observed. Starting from $r < 3$ associated with one stable value x, one observes a sequence of period doubling processes that follow at values of $r > 3$ and then lead to a chaotic regime at $r = 3.5699$. The growing factor r for the logistic map corresponds to the parameter d_0 here. For the two-mode RASER and with d_0 up to 10^{21}, only one chaotic regime has been identified in the present numerical simulations. At this stage, it is not clear whether or not there exists an analogy between the logistic map and the two-mode RASER. At very high values of $d_0 > 10^{21}$ further windows with n-fold period doublings or chaos may exist, or a new sort of chaos at specific values of d_0 may exists for the RASER that may have been missed in the current analysis. This warrants future investigations.

5. Experimental setup for SABRE and PHIP pumped ^{1}H RASER

Fig. 4(a) shows the low field NMR setup for the SABRE pumped RASER experiments [7]. A home-built electromagnet is used, whose cylindrical main coil combined with a set of four shim (x,

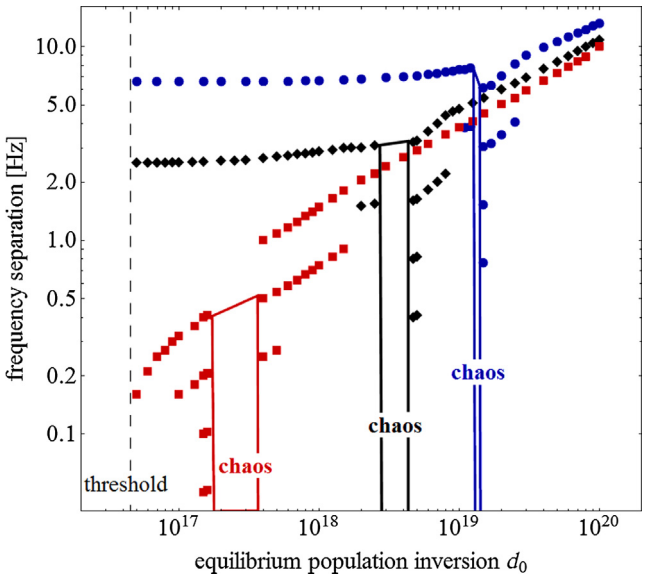

Fig. 3. Simulated frequency separation between successive lines of a two-mode RASER versus the equilibrium population inversion d_0. Circles (blue), diamonds (black) and squares (red) represent a splitting between the two modes at $|\nu_2 - \nu_1|$ = 7 Hz, 3.5 Hz and 2 Hz, respectively. The simulation parameters are: $\Gamma = 0.07\ s^{-1}$ for the pumping rate and $\gamma_m = 1/T_2^* = 7.7\ s^{-1}$, $T_1^{-1} = 0.07\ s^{-1}$, comparable to NMR relaxation parameters for organic molecules measured at 1.45 T [9]. The dashed line at $4.5 \cdot 10^{16}$ indicates the RASER threshold d_{th}. Red, black and blue polygons indicate the three chaotic regimes, where a continuum of frequency splittings characterizes the RASER spectrum. Close to the chaotic regimes one-, two- or three-fold period doublings occur which are represented by two, three or four points at 1/2, 1/4 or 1/8 of the frequency difference between two large lines (as seen in Fig. 2b). (For interpretation of the references to colour in this figure legend, the reader is referred to the web version of this article.)

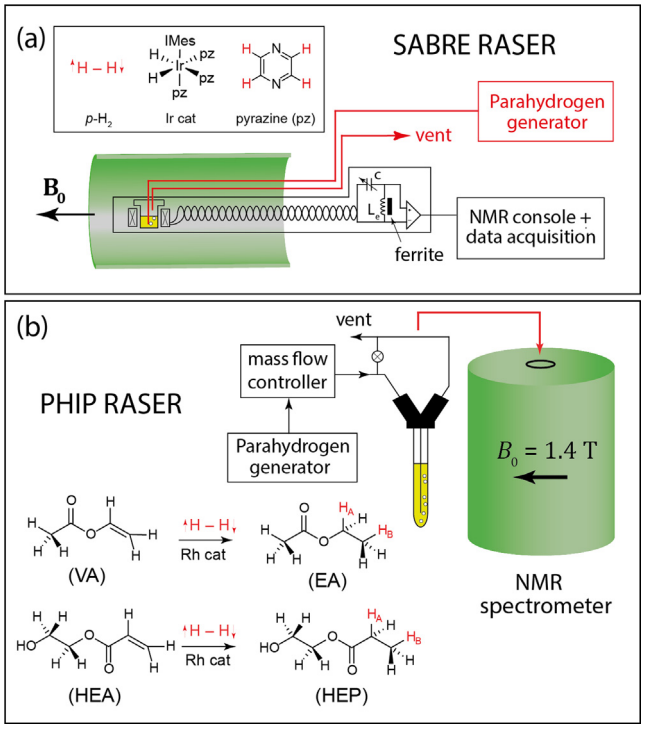

Fig. 4. Experimental setup of the SABRE and PHIP pumped RASER. (a) Schematic of the External High Quality Enhanced (EHQE) [6] NMR spectrometer (black), magnetic field system (B_0 = 3.9 mT, green), and p-H_2 generator (Bruker, enrichment = 0.9) including delivery system (red). Parahydrogen, the SABRE active catalyst and the substrate pyrazine are shown in the inset. The ^1H SABRE polarized pyrazine is RASER active and observed at 166 KHz in the presence of a continuous p-H_2 flow. (b) Experimental setup for the PHIP RASER. A home-build p-H_2 converter delivers nearly 100% p-H_2 gas into the samples, which are detected at 1.45 T. ^1H RASER activity of PHIP hyperpolarized ethyl acetate (EA) or hydroxyethylpropionate (HEP) is observed at 61.7 MHz. Bottom: Pairwise addition of p-H_2 of the starting material VA (vinyl acetate) and HEA (2-hydroxyethyl acrylate) into hyperpolarized EA and HEP in the presence of a Rh catalyst. H_A and H_B (red) denote the hyperpolarized protons. (For interpretation of the references to colour in this figure legend, the reader is referred to the web version of this article.)

y,z,z^2) coils produces a field in the range 1 mT < B_0 < 20 mT and with a homogeneity of 1 ppm over the sample volume $V_s = 0.4\,cm^3$. A cylindrical input coil (diameter = 10 mm) coupled to an external ferrite resonator (EHQE, $Q \sim 100$) [6] is used for detection of the ^1H RASER signals at $B_0 = 3.9$ mT ($\omega_0 = 2\pi\,166$ kHz). The damping rate for the low field setup is $\kappa_m = \omega_0/Q \approx 10^4\ s^{-1}$. Samples were prepared under inert gas conditions. Substrates and solvents were dried and degassed using standard Schlenk techniques. The SABRE sample inside the coil contained 400 µl d_4-methanol, as well as 0.8 mg [IrCl(cod)(IMes)] (cod = cyclooctadiene; IMes = 1,3-bis(2,4,6-trimethylphenyl)imidazole-2-ylidene) and 1 mg pyrazine. Before the RASER experiments the SABRE sample was activated at room temperature by bubbling with hydrogen. Parahydrogen (p-H_2) generated at 36 K (~90% p-H_2 fraction) was supplied at 5 bar and at a constant flow rate of 10 sccm through the liquid sample using a nozzle.

For PHIP RASER experiments (see Fig. 4(b)) a bench-top NMR spectrometer is used at 1.45 T field (Spinsolve Carbon 60, Magritek, New Zealand) [9]. At 61.7 MHz ^1H frequency and Q = 68 the damping rate is $\kappa_m = 5.7 \cdot 10^6\ s^{-1}$. For the hydrogenation reactions, solutions were employed with 0.4 M of respective substrate (vinyl acetate (VA), or 2-hydroxyl ethyl acrylate (HEA)), and 0.4 mM of catalyst [Rh(nbd)(dppb)]BF_4 (nbd = bicyclo-[2.2.1]hepta-2,5-diene; dppb = 1,4-bis(diphenylphosphino)butane) in d_4-methanol. The samples were filled into regular 5 mm NMR tubes. Parahydrogen (p-H_2) was bubbled though the solution at 75 °C and at 6.9 bar for 15 s to yield full conversion before transfer into the magnet. A home-built cryogenic generator [35] delivered nearly 100% p-H_2 at 150 sccm. The products resulting after hydrogenation are ethylacetate (EA) and 2-hydroxyethyl-propionate (HEP).

The data for both experimental setups were analyzed with a custom python script [7]. In order to suppress sideband effects, the RASER signals were multiplied by a hamming window with a predefined length before Fourier transformation. All presented RASER spectra are in magnitude mode.

All RASER signals and their corresponding spectra have been simulated in mathematica 8 from Wolfram Research using the built-in NDsolve function.

At this stage, we can estimate the expected effects for the RASER experiments at low and high field. For the SABRE pumped ^1H RASER at 3.9 mT the relevant parameters are $\gamma_m \approx 1\ s^{-1}$, $T_1^{-1} \approx 0.2\ s^{-1}$ and $\Gamma \approx 0.1\ s^{-1}$. Therefore, the first condition for adiabatic elimination $\kappa_m >> \gamma_m, T_1^{-1}, \Gamma$ applies but $\Gamma \approx \gamma_m \approx T_1^{-1}$ are of the same order of magnitude. The SABRE induced population inversion is estimated to be $d_0 \approx 2 \cdot 10^{16}$. Therefore, line collapse, frequency combs and initial stages of period doublings may be expected and have indeed been observed [8].

For the PHIP pumped RASER experiments at 1.4 T the relevant parameters are $\gamma_m = 7.7\,s^{-1}$ and $T_1^{-1} \approx \Gamma \approx 0.04 - 0.1\,s^{-1}$ so the condition for the first adiabatic elimination, $\kappa_m >> \gamma_m, T_1^{-1}, \Gamma$ holds but the second condition ($\Gamma >> \gamma_m$) is not fulfilled, since the opposite $\gamma_m >> T_1^{-1}, \Gamma$ is the case. Therefore, if the equilibrium population inversion d_0 is large enough, for the conducted PHIP RASER experiments no collapse phenomena should occur, instead, both,

multiple period doubling processes and chaos are expected. To estimate d_0, the ^{1}H polarization is measured prior to RASER action. We found the initial ^{1}H polarization to be $0.1 < P_H < 0.25$. At a sample volume of $V_s \approx 0.2$ cm^3, this corresponds to a population inversion in the range $1.4 \cdot 10^{19} < d_0 < 3.6 \cdot 10^{19}$. According to Fig. 3, at line splittings of 7 Hz d_0 is high enough to produce multiple period doublings and chaos.

6. Single mode ^{1}H RASER revivals with SABRE pumped pyrazine at 3.9 mT

Pyrazine is a good SABRE substrate that polarizes well, which has four magnetically equivalent protons, therefore it represents an ideal molecule for a single-mode RASER. The ^{1}H RASER action of pyrazine under three different pumping conditions measured at $B_0 = 3.9$ mT (166 kHz ^{1}H frequency) is shown in Fig. 5. The three contrasted cases are (a) exponential slow buildup of the pumping rate $\Gamma(t)$ until a maximum pumping rate Γ_0 is reached, (b) At the constant maximum pumping rate Γ_0 a gradient is applied until the maximum possible population inversion $d_{max} = d_0\,\Gamma_0/(\Gamma_0 + T_1^{-1})$ is reached. Initial RASER oscillations are observed after the gradient is turned off. (c) After pumping into d_{max} in the presence of a gradient, the gradient and the p-H_2 supply is switched off, leading to an exponentially decreasing $\Gamma(t)$ and subsequent RASER revivals are observed.

First, Fig. 5(a) shows the RASER buildup phase after starting the p-H_2 supply at $t = 0$. After $t = 20$ s typical initial relaxation oscillations are visible, which, after about 60 s, turn into a stationary RASER signal superimposed by slight amplitude fluctuations. Second, in Fig. 5(b), at 133 s < t < 163 s, a magnetic field or crusher gradient is applied in order to kill any RASER activity and to reach an equilibrium state with maximum possible population inversion d_{max}. A sequence of intensive and short RASER bursts is observed, which finally evolves into the same stationary state as observed in (a). Finally, in Fig. 5(c), a second crusher pulse is applied during 223 s < t < 257 s, so the maximum d_{max} and Γ_0 can be reestablished. At $t = 257$ s, the gradient as well as the p-H_2 supply are turned off and six RASER revivals with decreasing amplitude and increasing width are observed. According to the theory of Section 3 only one RASER burst is expected if the pumping rate is $\Gamma = 0$ after turning off the p-H_2 supply. However, in the present experiments, dissolved p-H_2 continues to produce hyperpolarization and Γ can be modeled with an exponential decay.

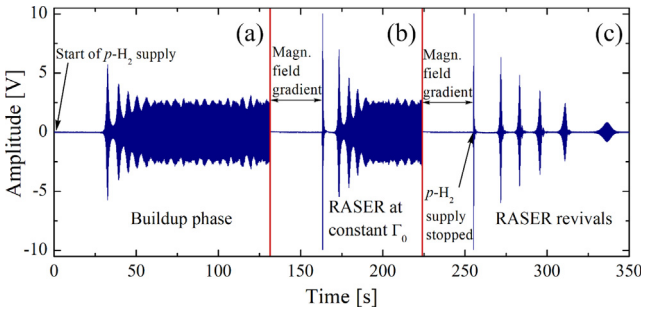

Fig. 5. ^{1}H RASER signal of SABRE hyperpolarized pyrazine measured at $B_0 = 0.039$ T (166 kHz) and three different pumping conditions. (a) Buildup phase: After the p-H_2 supply is switched on at $t = 0$ s, initial relaxation oscillations start at $t = 30$ s which evolve at late time into a stationary RASER signal. (b) After switching off a crusher gradient of 20 s length, a sequence of intense and short RASER bursts is observed which evolve into a stationary state. (c) After turning off both, the crusher gradient (20 s duration) and the p-H_2 supply, a sequence of six RASER revivals with decreasing amplitude and increasing width is observed. This agrees with the single-mode RASER theory if an exponentially decreasing pumping rate is assumed.

In order to explain the RASER action during an exponential buildup and decay of the pumping rate (Fig. 5(a) and (c)), we compare the measurements with simulations for increasing (Fig. 6(a)–(c)) and decreasing (Fig. 6(d)–(f)) pumping rate based on Eqs (7) and (8) in Section 3.

First, in Fig. 6(a)–(c) we discuss the case of exponentially increasing pumping rate $\Gamma(t) = \Gamma_0[1 - \exp(-t/\tau_p)]$: In Fig. 6(a), the experimentally measured initial relaxation oscillation is in full agreement with the simulation shown in Fig. 6(b). The specific simulation parameters are $\Gamma_0 = 0.021$ s^{-1} and $\tau_p = 21$ s with $\gamma_m = 1$ s^{-1}, $T_1^{-1} = 0.2$ s^{-1}, $d_0 = 5.5 \cdot 10^{16}$. The corresponding simulated population inversion d (Fig. 6(c)) increases from $0 < t < 21$ s until RASER action starts at $t \approx 20$ s.

Second, Fig. 6(d)–(f) show the case of exponentially decreasing pumping rate $\Gamma(t) = \Gamma_0 \exp(-t/\tau_r)$: The simulation of the six RASER revivals in Fig. 6(e) is in reasonable agreement with the measured signal in Fig. 6(d). Here, the simulation parameters are $\Gamma_0 = 0.066$ s^{-1}, $\tau_r = 21$ s, $\gamma_m = 1$ s^{-1}, $T_1^{-1} = 0.083$ s^{-1} and $d_0 = 1.7 \cdot 10^{17}$. The corresponding population inversion d versus time in Fig. 6(f) looks like an exponentially decaying saw-tooth with rapidly falling edges coinciding with the times when the RASER revivals occur. The increasing length of the revivals can be explained by inspection of Eq. (5), $dA/dt = \left[|g_m|^2\, d/\kappa_m - \gamma_m\right] A$, and introducing the total damping rate $\kappa_{tot} = |g_m|^2\, d/\kappa_m - \gamma_m$. In the beginning of the experiment d is large (Fig. 6(f)) as well as the amplitude A of the first revival (Fig. 6(e)). Therefore, $\kappa_{tot} >> 0$ and the RASER signal revival changes very quickly in time and appears as a short spike. At later times the value d where the burst occurs, has decreased substantially; the amplitude of the RASER revival is smaller and $\kappa_{tot} \to +0$. Therefore, the amplitude of the corresponding revival decreases with time and the width increases. The relatively long rate constants $\tau_p, \tau_r \sim 20$ s and the rather large separation in time between the RASER revivals can be explained by a long-lived reservoir for singlet state magnetization in the solution. For example, the singlet reservoir could be dissolved p-H_2 gas, which continues to hyperpolarize pyrazine via the employed SABRE catalyst. Another possibility for a long-lived reservoir is pyrazine molecules prepared in the singlet state. They transfer their singlet magnetization via the catalyst into RASER active negative magnetization. This question is subject of future investigations.

7. Experimental results of PHIP pumped ^{1}H RASER at 1.4 T

In this section we discuss two distinct hydrogenative PHIP ^{1}H-RASER experiments, the ALTADENA and PASADENA protocols, leading to two different polarization structures of the products. Both protocols, were executed after pairwise addition of p-H_2 gas to two distinct molecules, vinylacetate (VA) and hydroxyethyl acrylate (HEA) leading to ethyl acetate (EA) and 2-hydroxyethyl propionate (HEP), respectively (see Fig. 4(b)). Sections 7.1 and 7.2 presents thermally polarized and PHIP hyperpolarized NMR spectra of HEP and EA in order to analyze the spectra without RASER activity first. The two chosen substrates are well suited for analysis with the theory of Section 4: In a first approximation, the ALTADENA pumped RASER of HEP can roughly be described as a RASER based on two J-coupled lines, as we discuss in Section 7.3. In our ALTADENA protocol, p-H_2 addition to HEP is performed in the Earth's field, and the sample is transferred adiabatically into the bore of the 1.45 T benchtop Magritek magnet. A large negative polarization or equivalently a large population inversion is produced at one proton, H_B, of the CH_3 group in HEP. In Section 7.4 we show that a PASADENA pumped RASER of EA is an example, where the two modes are precise measures of the chemical shift

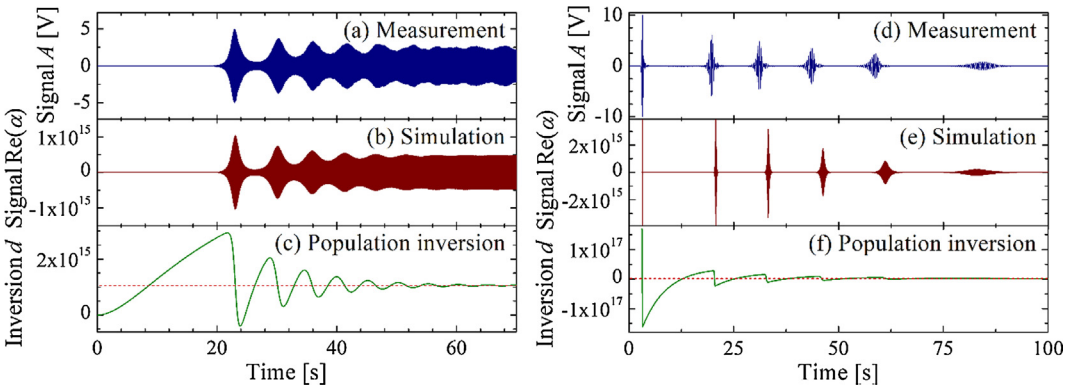

Fig. 6. Measured (a) and simulated (b) initial relaxation oscillations of the pyrazine ^{1}H RASER after turning on the *p*-H_2 supply. (c) Simulation of the corresponding population inversion *d* versus time. (d) Measured ^{1}H RASER revivals after switching off both, the crusher gradient and the *p*-H_2 supply. Six RASER revivals with decreasing amplitude and increasing width can be observed. The simulation in (e) is in reasonable agreement with the measurement in (d). The corresponding population inversion *d* versus time in (f) resembles an exponentially decreasing saw-tooth, which evolves towards zero. Red dotted lines in (c) and (f) indicate the RASER threshold $d_{th} = 1.1 \cdot 10^{15}$. See text for simulation parameters. (For interpretation of the references to colour in this figure legend, the reader is referred to the web version of this article.)

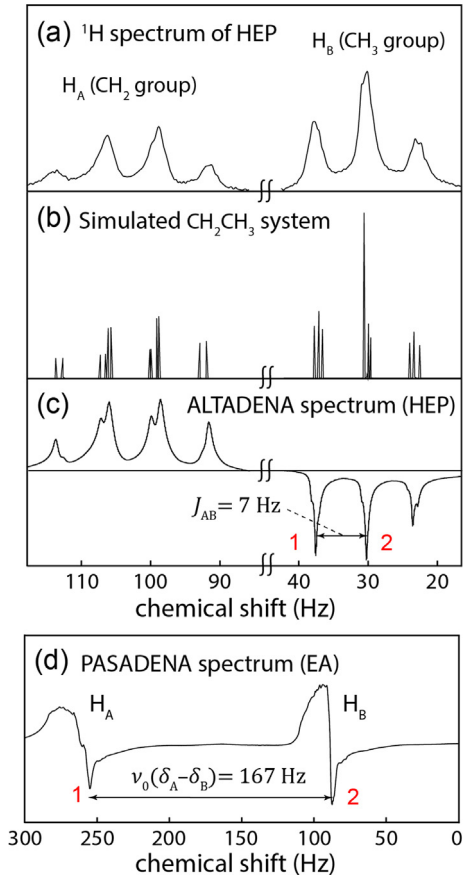

Fig. 7. NMR and PHIP spectra of HEP and EA at 1.45 T. (a–c) Triplet (CH_3-group) and a quartet (CH_2 group) of the ^{1}H NMR spectrum of HEP separated by a 1.2 ppm chemical shift difference (74 Hz @ 61.7 MHz). The splitting in each group is $J_{AB} = 7$ Hz. (a) Standard NMR spectrum (b) Simulated, high resolution NMR spectrum (line-width = 0.01 Hz) showing the fine splitting due to strong coupling effects. (c) ALTADENA PHIP ^{1}H spectrum. The two negative lines 1 and 2 (red) of the triplet with equal amplitudes are RASER active. (d) PASADENA PHIP ^{1}H spectrum of EA. The two lines with negative amplitude 1 and 2 (red) are RASER active. They are separated by the frequency difference of 2.7 ppm (=167 Hz). This measured separation might not represent the exact chemical shift difference (2.8 ppm) due to the broad linewidth. (For interpretation of the references to colour in this figure legend, the reader is referred to the web version of this article.)

difference between two lines in the NMR spectrum. For the PASADENA experiments, EA is hydrogenated inside the 1.45 T magnet. The resulting negative polarization in the case of PASADENA is located at both the H_A and the H_B protons of the CH_2 and CH_3 groups. For full experimental details see Joalland et al. [9].

7.1. NMR spectra of thermally and ALTADENA polarized HEP at 1.45 T.

The measured HEP (hydroxyethylpropionate) NMR spectrum in Fig. 7(a) shows an enhanced view of the triplet and quartet structures associated with the CH_3 (H_B) and the CH_2 (H_A) group, respectively. From this spectrum one can determine the *J*-coupling constant $J_{AB} = 7$ Hz and the line-width $\Delta_L = 1/(\pi T_2^*) = 2.45$ Hz, which corresponds to $T_2^* = 0.13$ s or $\gamma_m = 7.7\,s^{-1}$. The longitudinal relaxation time is $T_1 = 16$ s ($T_1^{-1} = 0.066\ s^{-1}$) while the chemical shift difference between the CH_3 and the CH_2 group is $|\delta_{CH3} - \delta_{CH2}| = 1.2$ ppm. At 1.45 T this corresponds to a ^{1}H frequency difference of 74 Hz. The ratio $J_{AB}/|\delta_{CH3} - \delta_{CH2}| \approx 0.1$ indicates the beginning of the strong coupling regime. In this regime there is a fine splitting, which is shown in the simulation of the CH_2-CH_3 system in Fig. 7(b). The total number of lines is $4 \times 4 = 16$ for the CH_3 group and $2 \times 6 = 12$ for the CH_2 group [36,37]. In the simulation in 7(b) a line-width of 0.01 Hz is assumed, which is insufficient to resolve all 28 lines in the spectrum. The largest fine splitting is about 0.9 Hz in the quartet and 0.6 Hz in the triplet. These largest fine splittings become visible in the ALTADENA PHIP spectrum of HEP in Fig. 7(c). Note, the negative and positive sign of the triplet (H_B) and quartet (H_A), respectively. Since proton H_B is found to be RASER active, the three lines of the H_B group are associated with population inversion and, thus, negative amplitudes. Experiments show that the two inner lines of the triplet with equal amplitudes and separated by $J_{AB} = 7$ Hz, denoted by 1 and 2 in Fig. 7(c), are both RASER active, while the third line with half the amplitude is RASER inactive. Here we assume, that the two RASER active lines suppress RASER activity of the third smaller line. Therefore, in the ALTADENA pumped ^{1}H-RASER spectrum of HEP, two lines separated by 7 Hz are expected. We postulate that the polarization of the smaller third line serves as a reservoir, which pumps the two other RASER active lines through cross-relaxation with a maximum pumping rate of $\Gamma_0 \approx 0.05 - 0.2\ s^{-1}$. We assume that Γ_0, after turning off the *p*-

H_2 supply and transfer into the magnet, decays exponentially as $\Gamma = \Gamma_0 \exp(-t/\tau_r)$, where the decay rate $0.04\,s^{-1} < \tau_r^{-1} < 0.15\,s^{-1}$ is in the order of T_1^{-1}. This means that RASER revivals are expected here, similar to the ones for the single-mode pyrazine RASER discussed in Section 3. Since the amplitudes of all lines in the quartet (H_A) in Fig. 7(c) are positive (no population inversion), none of the quartet lines can be RASER active. Therefore, for HEP no chemical shift information can be measured with the ALTADENA pumped ^{1}H RASER .

7.2. NMR spectra of thermally and PASADENA polarized EA at 1.4 T

In the same way as in Section 7.1 thermally polarized NMR spectra for EA (ethylacetate) have been measured at 1.45 T (not shown in Fig. 7). The measured NMR parameters are: $T_1 = 25$ s ($T_1^{-1} = 0.04$ s^{-1}), $|\delta_{CH3} - \delta_{CH2}| = |\delta_{HA} - \delta_{HB}| = 2.8$ ppm. At 1.45 T $|\delta_{CH3} - \delta_{CH2}| = 2.8$ ppm corresponds to a ^{1}H frequency difference of 174 Hz. The ratio $J_{AB}/|\delta_{CH3} - \delta_{CH2}| = 0.042$ indicates the intermediate regime between weak- and strong-coupling with very small sub-splittings, which cannot be resolved in the NMR or the PHIP spectra.

Fig. 7(d) shows the PASADENA NMR spectrum of EA. The typical antiphase spectrum is modified, since the positive peaks are very broad in contrast to the two, narrow negative peaks, which are separated by the chemical shift difference of 167 Hz. The narrow peaks can be explained by the total damping $\kappa_{tot} = |g_m|^2 d/\kappa_m - \gamma_m$, which close to threshold is small for positive d (narrow negative peaks) and large for negative d (broad positive peaks). The two negative peaks in 7(d) become RASER active once the threshold d_{th} is surpassed. Therefore, for the PASADENA pumped ^{1}H-RASER of EA, both, the chemical shift difference of 167 Hz and the splitting due to the J-coupling ($J_{AB} = 7$ Hz) can be measured.

7.3. ALTADENA ^{1}H RASER of HEP

An example for an ALTADENA-RASER signal of HEP (hydroxyethylpropionate) is shown in Fig. 8(a). In the first 10 s, the RASER signal exhibits several bursts or revivals, which have a length of about 1 – 2 s and whose detailed shape is complicated. For 10 s < t < 22 s, the amplitude of the successive RASER revivals decrease while the width increases with time. This is similar to the RASER revivals of the single-mode RASER detailed in Section 6. At t > 20 s, the RASER signal turns into a free induction decay with prolonged duration. A Fourier transformation of the whole RASER signal is not advisable, since the properties of the RASER revivals change with time. In order to analyze the spectral features, the RASER signal is divided into five time slices of 2 s duration, which are indicated by panels I-V in Fig. 8(a). The individual windows are multiplied by a Hamming filter to yield a compromise between sufficient spectral resolution, stationarity of the signal and avoiding sideband artifacts caused by Fourier transformation of several RASER bursts. A series of five spectra corresponding to the five windows I-V is shown in Fig. 8(b). The first spectrum I, Fourier transformed from 0 to 2 s, has a width of about 80 Hz and has no resolved features. The broad spectrum is caused by a rapid decrease of the population inversion leading to a very short spike (window I in Fig. 8(a)). The second spectrum II, Fourier transformed from 2 s to 4 s, shows more interesting features: Two major lines separated by 7.3 Hz are visible together with several other lines located at frequencies of exactly 1/2, 1/3, 1/4 and 1/8 of the base splitting of 7.3 Hz. We believe spectrum II is the result of multiple period doubling processes and has chaotic features, because the number of lines increases when increasing the length of the window. Many other ALTADENA and PASADENA RASER experiments have been performed, which are not shown here, but which have similar period doubling and chaotic features in the first seconds of RASER action. All these chaotic spectra are very different from one another, which is fascinating but may be expected because any chaotic trajectory will have completely different outcomes despite very close initial conditions. Spectrum III, taken from 6 s to 8 s, is a frequency comb with several side bands and a frequency difference of 7 Hz between the two major lines. In spectrum IV (12.5 – 14.5 s), the sidebands of the frequency comb have vanished and two lines separated by $J_{AB} = 7$ Hz remain. Note that the left line in this doublet has a higher amplitude. Finally, in spectrum V (18 s – 20 s) the right line has died out and only one line at 330 Hz offset frequency remains. Several reasons could be

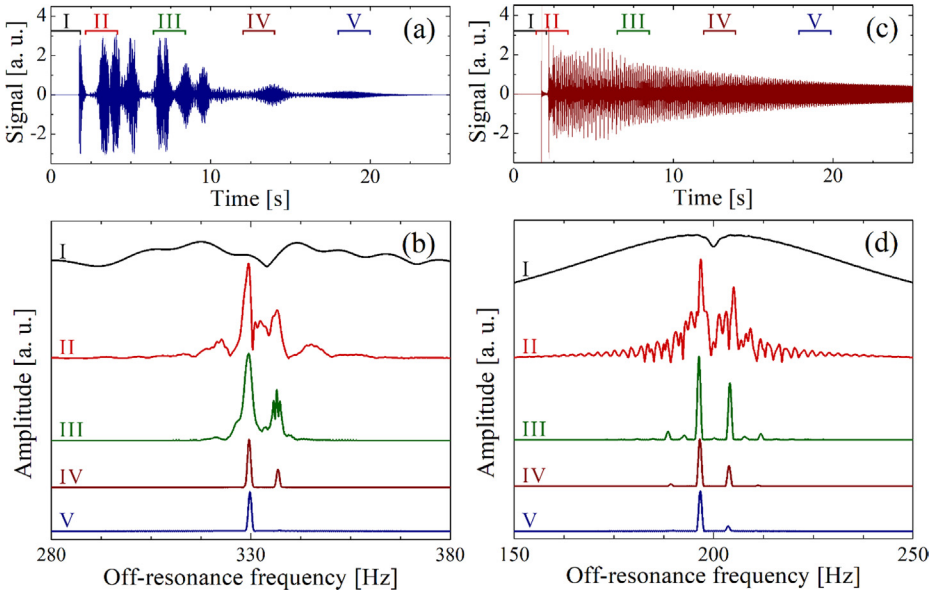

Fig. 8. Measured (a,b) and simulated (c,d) ALTADENA ^{1}H RASER of HEP at 1.45 T. (a) Measured ^{1}H RASER signal versus time. Five time windows of 2 s length are indicated by I-V. (b) Stack plot of five RASER spectra obtained after Fourier transformation of the windows in (a). The broad spectrum I is followed by a frequency comb like spectrum II with chaotic features and split by multiple period doublings. Spectrum III displays a frequency comb, while spectrum IV is a doublet spaced by 7 Hz. Finally, in spectrum V a single line remains. (c) Simulation of a two-mode RASER signal assuming an exponential decay of the population inversion. (d) Corresponding stack plot of five simulated RASER spectra obtained from the five time slices in (c). The simulations reflect the basic features of the measured spectra shown in (b). See text for simulation parameters.

responsible for disappearance of the right line: Either the longitudinal relaxation times of both modes $T_{1,1}$ and $T_{1,2}$ are not exactly the same and/or the pumping rates Γ_1 and Γ_2 differ slightly. The corresponding simulated RASER signal of the ALTADENA pumped HEP is shown in Fig. 8(c). To test the line vanishing effect via simulation, we assume two RASER modes separated by 7 Hz, using the measured NMR parameters for HEP ($\gamma_m = 7.7 s^{-1}$, $T_1^{-1} = 0.0625 s^{-1}$, $J_{AB} = 7 Hz$), and set $\Gamma_0 = 0.093\ s^{-1}$, $d_0 = 1.43 \cdot 10^{19}$ for both modes and, finally chose two slightly different values for the decay constants $\tau_r^{-1} = 0.099 s^{-1}$ and $0.1 s^{-1}$ for the two modes. Notice that the simulation only uses two interacting RASER modes, whereas the experimental HEP ALTADENA spectrum is much more complex, involving twelve possible RASER active modes. Therefore, the simulated RASER signal in Fig. 8(c) cannot be expected to be a perfect match of the experimental result in Fig. 8(a). Nonetheless, complex experiment and oversimplified simulation share some key features in the time and frequency domains. In the time domain, the shared features are the initial short burst and the chaotic regime in the first few seconds. In the frequency domain, the similarity between experiment and simulation is much more pronounced. Fig. 8(d) shows the corresponding series of five Fourier spectra with 2 s Hamming windows chosen at the same time intervals as in Fig. 8(a). Spectrum I is broad (width ~100 Hz) and featureless, just like the experimental spectrum in Fig. 8(b). Spectrum II in Fig. 8(d) shows several period doublings and is similar to the measured spectrum II in Fig. 8(b). In addition, the simulated spectra III, IV and V consecutively change from a frequency comb with one-fold period doubling into two lines of unequal intensity separated by 7 Hz. The experimental spectra show the same behavior. In conclusion: The two-mode RASER theory, assuming 7 Hz line splitting and an initial $d_0 \approx 1.5 \cdot 10^{19}$ which decays exponentially with time, predicts a sequence of RASER spectra, which change from initial chaos into a period doubled frequency comb, then into a two-line spectrum and finally into a single line spectrum. This sequence is in remarkably good agreement with the measured HEP RASER spectrum.

7.4. PASADENA ^{1}H RASER activity of EA

Up to now, we have shown ALTADENA pumped RASER spectra that do not contain any chemical shift information. According to Section 7.2 chemical shift and *J*-coupling information may be expected for the PASADENA pumped RASER. Fig. 9 shows the results for the ^{1}H PASADENA RASER of EA (ethylacetate) hyperpolarized in the 1.45 T magnet. Fig. 9(a) is a plot of the complete RASER signal versus time, which consists of a sequence of eight RASER bursts or revivals. The chemical shift information of the RASER active protons H_A and H_B, whose resonance frequencies differ by 167 Hz (2.7 ppm) at 1.45 T, are encoded in an intriguing way. Consider the expanded view of the first RASER revival I depicted in Fig. 9(b). In the first 330 ms ($9.5\ s < t < 9.83\ s$) the RASER signal oscillates with an offset frequency of 100 Hz. Then, at $t = 9.83$ s the signal jumps into a second mode within a few ms, which oscillates with an offset frequency of 267 Hz for about 400 ms. For $t > 10.25$ s, the signal alternates in a random fashion between the two resonances of H_A (100 Hz) and H_B (267 Hz). Additionally, there are periods of time where both oscillations are superimposed. These statistical jumps are so-called intermittence phenomena. The spectrum of the entire window in Fig. 9(b) shows two groups separated by the chemical shift difference of 167 Hz (see Fig. 9(c)). Each sub-spectrum, associated with H_A and H_B, has frequency comb like features. Especially the spectrum of H_B at 267 Hz con-

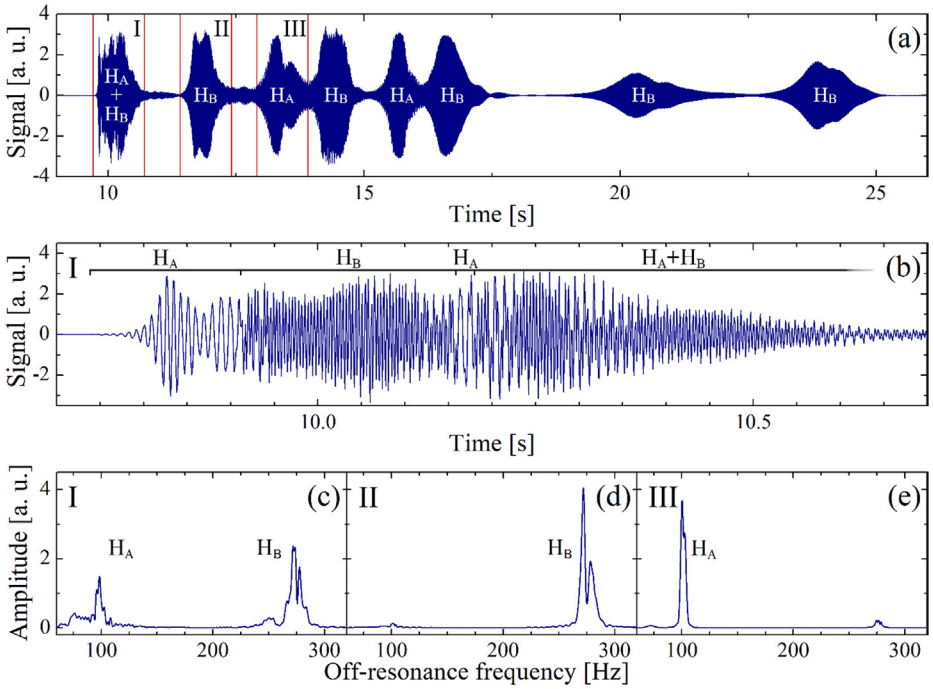

Fig. 9. Measured PHIP hyperpolarized ^{1}H RASER of EA prepared by the PASADENA protocol. H_A and H_B refers to the protons of the CH_3 and CH_2 groups of EA, respectively. (a) RASER revivals versus time with highlighted time windows of 2 s lengths (I, II and III). (b) Enhanced view of the first RASER revival I in (a). Over the entire time, the frequency of the RASER oscillation is jumping in an irregular way between two offset frequencies assigned to 100 Hz and 267 Hz. The difference of 167 Hz corresponds to the chemical shift difference of 2.8 ppm between H_A and H_B. (c–e) Fourier spectra of the time slices I-III shown in the absolute mode. (c) The spectrum of the entire window I features two frequency comb like structures separated by 167 Hz. (d) The spectrum of window II is dominated by two lines centered at 267 Hz (H_B) and separated by $J_{AB} = 7$ Hz. (e) The spectrum of window III shows mainly one line at 100 Hz offset frequency corresponding to H_A. All further RASER revivals in (a) change from 100 Hz (H_A) to 267 Hz (H_B) offset frequency and vice versa until at $t > 16$ s the frequency of H_B remains (spectra not shown).

tains further sub-splittings, probably caused by period doubling. The intermittence phenomenon, which is present in RASER revival I, disappears in all following revivals. Instead the H_A and H_B resonances are jumping back and forth between successive RASER revivals. For example the spectrum from window II in Fig. 9(d) consists of a doublet with a spacing of $J_{AB} = 7$ Hz and centered at the H_B resonance at 267 Hz. The signal from H_A is small, probably because its population inversion is suppressed while H_B is RASER active. The change of resonance H_B from a frequency comb in 9(c) into a doublet in 9(d) can be explained by the decay of polarization, as described above for the ALTADENA-RASER. The spectrum in Fig. 9 (e) has its main peak at 100 Hz, which is the line position of H_A and a small group of lines at the resonance frequency of H_B can be identified. With each successive RASER revival, the line position continues to change back and forth from 100 Hz to 267 Hz and vice versa. For $t > 16$ s, only H_B is RASER active. The back and forth jumps between two frequencies for successive revivals might be explained by an oscillating behavior of the saw-tooth like population inversion of the two RASER modes. While one mode is RASER active, decreasing its own population inversion the population inversion of the other non RASER active mode is recovering until it becomes RASER active. Further simulations are needed for a detailed understanding of the combined intermittence and revival phenomena of multiple modes.

In conclusion, while the ALTADENA pumped RASER spectra shows line splittings due to *J*-coupling, the PASADENA RASER spectra can measure both, chemical shift differences as well as *J*-couplings. In the future, a continuous flow supply of *p*-H_2 is envisioned, which produces a constant and adjustable polarization in the absence of any bubbles. With such a delivery system, the relevant NMR parameters, as well as all reported non-linear effects could be measured with much higher precision.

8. Conclusion

In this contribution, we have introduced the basic building blocks to describe many phenomena occurring in multi-mode RASERs, which can be described as a non-linear coupled spin system pumped into a state of population inversion. The RASER phenomena are described with strategies used in synergetics and non-linear mathematics. The key phenomena comprise RASER revivals, line collapse, substantial shifts in *J*-coupling or chemical shift induced splittings, frequency combs, period doubling processes and, finally, chaos. We have shown that SABRE and PHIP pumped RASERs are excellent tools for the experimental investigation of these phenomena. SABRE and PHIP pumped RASERs deliver precise information for analysis, but also feature comparatively simple setups as opposed to He or Xe MASERS for example.

9. Future perspectives and applications

The understanding of the non-linear effects in RASERs is essential when considering various applications in the future. For example, in NMR RASER spectroscopy, the goal is high precision measurement of chemical shifts and *J*-coupling constants. However, non-linear effects in RASERs may render accurate measurement of these NMR parameters difficult. Since the non-linear effects grow with the equilibrium population inversion d_0, the aim would be to reduce the RASER threshold d_{th} as much as possible:

Assuming $\Gamma > T_1^{-1}$ and using Eq. (5) the threshold condition is given by $R = |g_m|^2 d_{th}/\kappa_m = \gamma_m$. For a spin species X with gyromagnetic ratio γ_X, the threshold for a single-mode RASER is

$$d_{th} = \frac{\gamma_m \kappa_m}{|g_m|^2} = \frac{4V_s}{\mu_0 \hbar \eta \gamma_X^2 T_2^* Q}. \quad (20)$$

The filling factor $0 < \eta < 1$ is introduced in Eq. (20) as a loss factor, because the coil volume V_c is usually larger than the sample volume V_s. Eq. (20) predicts that d_{th} is small if Q is high, if η is close to one and if the sample volume V_s is small.

The factor $\gamma_X^2 T_2^*$ in Eq. (20) deserves a closer inspection. Let us assume a homogeneous field and isotopically enriched, liquid NMR samples containing ^{15}N and protons. In this case, $\gamma_{15N}^2 T_{2,15N}^*$ is not significantly different compared to $\gamma_H^2 T_{2,H}^*$, since $T_{2,H}^* \propto 1/(\gamma_H \gamma_H)^2$ and the dipolar cross relaxation time $T_{2,15N}^* \propto 1/(\gamma_H \gamma_{15N})^2$ is a factor of $\gamma_{15N}^2/\gamma_H^2 \approx 0.01$ smaller. This is different for a sample with pure ^{15}N, since in this case $T_{2,15N}^* \propto 1/(\gamma_{15N} \gamma_{15N})^2$. Consequently, the threshold d_{th} is about 100 times smaller compared to a sample containing both ^{15}N and ^{1}H. For clarity, we have not considered the distance between the ^{15}N and ^{1}H spins, which makes the difference between the two cases even larger. The necessary population inversion on ^{15}N or other hetero-nuclei can be produced for example by the SABRE SHEATH-method [38–40]. In conclusion, for pure ^{15}N samples very high precision RASER spectroscopy nearly free from non-linear effects should be viable.

This analysis is more dramatic when considering a pure electron-spin based RASER, for example for the electron spins in optically pumped NV centers [41–45]. Here, the samples are small diamonds with typical volumes ranging from 1 μm^3 to 1 mm^3. Actually, for mm^3 sized samples the coupling constant for electrons is $|g_m^e| = \gamma_e \sqrt{\mu_0 \hbar \omega_0 / 4 V_s} \approx 10\ s^{-1}$, which is more than five orders of magnitude larger compared to ^{1}H samples with $V_s = 0.4\ cm^3$. Using typical values of $T_2^* \propto 0.5ms$ for the electron spins in NV centers, assuming $Q \sim 1000$ and high electron spin polarization $P_e \sim 1$, this means very small electron spin RASER devices should be viable using only 10^6–10^9 electron spins. A RASER could operate with only one to 1000 electrons, if the *Q* factor is increased further, say to 10^6 for instance by active removal of the damping of the LC resonator, using an external negative impedance [46]. This opens up new perspectives for QCD effects [1] in RASER resonators and for micro electronic devices, where tiny RASER oscillators embedded in microchips with tunable quality factors ($10 < Q < 10^6$) can produce either regular oscillations or possibly chaotic signals (true random generators).

Such electron-spin or nuclear-spin based RASERs could be useful as precise spin clocks [47] in fundamental physics [47,48], as sensors of external magnetic fields or of rotations [8,49–52] or as random number generators for message encryption [15]. Furthermore, nuclear- and electron-spin based RASERs can be used as ultra-low noise preamplifiers for very weak electromagnetic signals, which operate in a broad frequency regimes ranging from 2 kHz < ν < 20 GHz. For example, RASER amplifiers could detect very weak NMR signals originating from rare spins (^{13}C, ^{33}S or ^{57}Fe) of biological samples or even living beings. This may open new possibilities for biological and clinical NMR and MRI as well as material sciences.

Up to now, we have shown self-organizing phenomena (i.e. line collapse, period doubling, intermittence and chaos), which arise in a multi-mode RASER in the time and in the frequency domain. The next step will be to investigate self-organized multi-mode RASER action in space and time. This means that Eqs. (1)–(3) have to be extended into a set of non-linear coupled partial differential equations in space and time. In general, these are quite complicated and exact solutions exists in some cases. Examples in chemistry and biology are chemical waves, reaction diffusion models or cell differentiation (morphogenesis) [13]. Similarly, the different modes

of a RASER could evolve in the (x, t)-dimension into soliton-like modes which are stable in time and do not interfere between each other. This would explain the spatial and temporal coexistence between different RASER modes with different amplitudes and initial conditions, which is outside the scope of the model in Eqs. (1)–(3). This would be a step forward for the understanding of how in the universe individual structures form on the microscopic (i.e. elementary particles) or on the macroscopic level. For another reason the inclusion of the spatial dimension into the model of RASER activity could be interesting for applications in magnetic resonance imaging. In the presence of a magnetic field gradient and in the absence of any external radio frequency fields RASER burst or revivals could form up, which may allow to measure the spatial spin density distribution in the sample. The physics of RASER imaging and its applications are currently in progress and will be published soon.

Finally, a set of N coupled miniaturized RASER oscillators might constitute an array of coupled qubits. The main problem of decoherence may be alleviated or completely absent [48,53]. Whether such a device is useful as a synergetic or a quantum computer [54–56] is still an open question.

Declaration of Competing Interest

The authors declare that they have no known competing financial interests or personal relationships that could have appeared to influence the work reported in this paper.

Acknowledgements

S.A. acknowledges support from Forschungszentrum Jülich and RWTH Aachen University. The authors thank Martin Süfke and Arne Kentner for providing the hardware and software used to capture and analyze the data. Research reported in this publication was supported by the National Institute of Biomedical Imaging and Bioengineering of the NIH under R21EB025313. We also acknowledge support from the North Carolina Biotechnology Center Translational Research Grant, as well as funding from the Mallinckrodt Foundation. E.Y.C. thanks the following for funding support: NSF CHE-1904780, National Cancer Institute under 1R21CA220137, and DOD CDMRP W81XWH-15-1-0271.

Author Contributions

S.A. supervised the project, wrote the original draft, developed the theory and simulated the experimental results. S.A, S.L. and T.T. formulated and designed the SABRE RASER experiments. S.L. and S.F. prepared SABRE samples. S.A., S.L, and S.F. conducted the SABRE pumped RASER experiments, analyzed the data and made the figures. E.Y.C. supervised the PHIP RASER experiments and provided crucial data including those showing chaos and intermittence. B.J. and N.A. prepared PHIP samples and conducted the ALTADENA and PASADENA PHIP/RASER experiments. S.A., S.L., S. F., E.Y.C. and T.T. reviewed and corrected the manuscript.

Appendix A. Supplementary data

Supplementary data to this article can be found online at https://doi.org/10.1016/j.jmr.2020.106815.

References

[1] S. Haroche, J.-M. Raimond, Exploring the Quantum, Oxford University Press, US, 2006.
[2] C.H. Townes, 1964 Nobel lecture: production of coherent radiation by atoms and molecules, Ieee Spectrum 8 (1965) 30–43.
[3] M. Sargent, M.O. Scully, W.E. Lamb, Laser Physics, Addison-Wesley Pub. Co. Advanced Book Program, 1976.
[4] T.H. Maiman, R.H. Hoskins, I.J. D'Haenens, C.K. Asawa, V. Evtuhov, Stimulated optical emission in fluorescent solids. II. Spectroscopy and stimulated emission in ruby, Phys. Rev. 4 (1961) 1151–1157.
[5] H. Haken, Laser, BI-Wiss.-Verlag, Leipzig, Mannheim, Wien, Zürich, 1995.
[6] M. Suefke, A. Liebisch, B. Blümich, S. Appelt, External high-quality-factor resonator tunes up nuclear magnetic resonance, Nat. Phys. 9 (2015) 767–771.
[7] M. Suefke, S. Lehmkuhl, A. Liebisch, B. Blümich, S. Appelt, Para-hydrogen raser delivers sub-millihertz resolution in nuclear magnetic resonance, Nat. Phys. 6 (2017) 568–572.
[8] S. Appelt, A. Kentner, S. Lehmkuhl, B. Blümich, From LASER physics to the para-hydrogen pumped RASER, Prog. Nucl. Mag. Res. Sp. 1–32 (2019).
[9] B. Joalland, N. Ariyasingha, S. Lehmkuhl, T. Theis, S. Appelt, E.Y. Chekmenev, Parahydrogen-induced radio amplification by stimulated emission of radiation, Angew. Chem. Int. Edit. 22 (2020) 8654–8660.
[10] A.N. Pravdivtsev, F.D. Sönnichsen, J.B. Hövener, Continuous radio amplification by stimulated emission of radiation using parahydrogen induced polarization (PHIP-RASER) at 14 Tesla, ChemPhysChem 7 (2020) 667–672.
[11] R.R. Ernst, G. Bodenhausen, A. Wokaun, Principles of Nuclear Magnetic Resonance in One and Two Dimensions, Clarendon Press, 1990.
[12] M. Porneuf, M. Goldman, NMR and More: In Honour of Anatole Abragam, Editions de Physique, 1994.
[13] H. Haken, Synergertics: An Introduction, Springer-Verlag, Berlin, Heidelberg, New York, Tokyo, 1983.
[14] H. Haken, Advanced Synergetics: Instability Hierachies of Self-Organizing Systems and Devices, Springer, Berlin, Heidelberg, New York, Tokyo, 1983.
[15] S.H. Strogatz, Nonlinear Dynamics and Chaos: With Applications to Physics, Biology, Chemistry, and Engineering, Avalon Publishing, 2014.
[16] R.W. Adams et al., Reversible interactions with para-hydrogen enhance NMR sensitivity by polarization transfer, Science 5922 (2009) 1708–1711.
[17] R.W. Adams, S.B. Duckett, R.A. Green, D.C. Williamson, G.G. Green, A theoretical basis for spontaneous polarization transfer in non-hydrogenative parahydrogen-induced polarization, J. Chem. Phys. 19 (2009) 194505.
[18] R.A. Green et al., The theory and practice of hyperpolarization in magnetic resonance using parahydrogen, Prog. Nucl. Mag. Res. Sp. 1–48 (2012).
[19] C.R. Bowers, D.P. Weitekamp, Transformation of symmetrization order to nuclear-spin magnetization by chemical reaction and nuclear magnetic resonance, Phys. Rev. Lett. 21 (1986) 2645–2648.
[20] C.R. Bowers, D.P. Weitekamp, Parahydrogen and synthesis allow dramatically enhanced nuclear alignment, J Am. Chem. Soc. 18 (1987) 5541–5542.
[21] J. Natterer, J. Bargon, Parahydrogen induced polarization, Prog. Nucl. Mag. Res. Sp. 4 (1997) 293–315.
[22] S.B. Duckett, C.J. Sleigh, Applications of the parahydrogen phenomenon: a chemical perspective, Prog. Nucl. Mag. Res. Sp. 1 (1999) 71–92.
[23] C.L. Tang, On maser rate equations and transient oscillations, J. Appl. Phys. 10 (1963) 2935–2940.
[24] M.G. Richards, B.P. Cowan, M.F. Secca, K. Machin, The He-3 nuclear zeeman maser, J. Phys. B. - At. Mol. Opt. 4 (1988) 665–681.
[25] T.E. Chupp, R.J. Hoare, R.L. Walsworth, B. Wu, Spin-Exchange-Pumped He-3 and Xe-129 Zeeman Masers, Phys. Rev. Lett. 15 (1994) 2363–2366.
[26] A.W. Overhauser, Polarization of nuclei in metals, Phys. Rev. 2 (1953) 411–415.
[27] A.J. Pell, G. Pintacuda, C.P. Grey, Paramagnetic NMR in solution and the solid state, Prog. Nucl. Mag. Res. Sp. (2018) 1–271.
[28] M.A. Bouchiat, T.R. Carver, C.M. Varnum, Nuclear polarization in He-3 gas induced by optical pumping and dipolar exchange, Phys. Rev. Lett. 8 (1960) 373–375.
[29] W. Happer, Optical-pumping, Rev. Mod. Phys. 2 (1972) 169–249.
[30] S. Appelt et al., Theory of spin-exchange optical pumping of He-3 and Xe-129, Phys. Rev. A 2 (1998) 1412–1439.
[31] W. Happer, Y.Y. Jau, T. Walker, Optically Pumped Atoms, Wiley, 2010.
[32] H.Y. Chen, Y. Lee, S. Bowen, C. Hilty, Spontaneous emission of NMR signals in hyperpolarized proton spin systems, J. Magn. Reson. 2 (2011) 204–209.
[33] L. Borkowski, A. Stefanski, FFT bifurcation analysis of routes to chaos via quasiperiodic solutions, Math. Probl. Eng. 1–9 (2015).
[34] A. Winnacker, Physik von Maser und Laser, Bibliographisches Institut, 1984.
[35] B. Feng, A.M. Coffey, R.D. Colon, E.Y. Chekmenev, K.W. Waddell, A pulsed injection parahydrogen generator and techniques for quantifying enrichment, J. Magn. Reson. 1 (2012) 258–262.
[36] S. Appelt et al., Paths from weak to strong coupling in NMR, Phys. Rev. A 2 (2010) 023420.
[37] S. Appelt, W.F. Häsing, H. Kühn, B. Blümich, Phenomena in J-coupled nuclear magnetic resonance spectroscopy in low magnetic fields, Phys. Rev. A 2 (2007) 023420.
[38] T. Theis et al., Microtesla SABRE enables 10% nitrogen-15 nuclear spin polarization, J. Am. Chem. Soc. 4 (2015) 1404–1407.
[39] M.L. Truong et al., ^{15}N hyperpolarization by reversible exchange using SABRE-SHEATH, J. Phys. Chem. C 16 (2015) 8786–8797.
[40] J.F. Colell et al., Generalizing, extending, and maximizing nitrogen-15 hyperpolarization induced by parahydrogen in reversible exchange, J. Phys. Chem. C 12 (2017) 6626–6634.
[41] J.F. Barry et al., Sensitivity optimization for NV-diamond magnetometry, Rev. Mod. Phys. 1 (2020).

[42] H.J. Mamin et al., Nanoscale nuclear magnetic resonance with a nitrogen-vacancy spin sensor, Science 6119 (2013) 557–560.
[43] T. Staudacher et al., Nuclear magnetic resonance spectroscopy on a (5-nanometer)^3 sample volume, Science 6119 (2013) 561–563.
[44] J.M. Taylor et al., High-sensitivity diamond magnetometer with nanoscale resolution, Nat. Phys. 10 (2008) 810–816.
[45] J. Wrachtrup, A. Gruber, L. Fleury, C. von Borczyskowski, Magnetic resonance on single nuclei, Chem. Phys. Lett. 1–2 (1997) 179–185.
[46] J. Anders, K. Lips, MR to go, J. Magn. Reson. (2019) 118–123.
[47] W. Heil et al., Spin clocks: probing fundamental symmetries in nature, Ann. Phys.-Berlin 8–9 (2013) 539–549.
[48] W. H. Zurek, Decoherence and the transition from quantum to classical – Revisited, arXiv:quant-ph/0306072, 2003.
[49] H. Gilles, Y. Monfort, J. Hamel, 3He maser for earth magnetic field measurement, Rev. Sci. Instrum. 10 (2003) 4515–4520.
[50] I.K. Kominis, T.W. Kornack, J.C. Allred, M.V. Romalis, A subfemtotesla multichannel atomic magnetometer, Nature 422 (2003) 596–599.
[51] M. Mehring, S. Appelt, B. Menke, P. Scheufler, The Physics of NMR-Gyroscopes, in: K. Linkwitz, U. Hangleiter (Eds.), High Precision Navigation, Springer Verlag, Berlin, Heidelberg, 1989, pp. 556–570.
[52] T.W. Kornack, R.K. Ghosh, M.V. Romalis, Nuclear spin gyroscope based on an atomic comagnetometer, Phys. Rev. Lett. 23 (2005) 230801.
[53] H.D. Zeh, On the interpretation of measurement in quantum theory, Found. Phys. 1 (1970) 69–76.
[54] H. Haken, Neural and Synergetic Computers, Springer-Verlag, Berlin, Heidelberg, 1988.
[55] D.P. Divincenzo, Quantum Computation, Science 5234 (1995) 255–261.
[56] J.A. Jones, Quantum computing with NMR, Prog. Nucl. Mag. Res. Sp. 2 (2011) 91–120.